Geochemistry, Geophysics, Geosystems®

AGU ADVANCING EARTH AND SPACE SCIENCE

RESEARCH ARTICLE
10.1029/2022GC010359

Key Points:

- The newly updated and publicly available CitcomSVE is highly accurate and efficient for modeling GIA and tidal loading problems
- CitcomSVE achieves second order accuracy in spatial resolution but its solutions are insensitive to time resolution
- CitcomSVE achieves >75% parallel computing efficiency for using up to 6,144 CPU cores

Supporting Information:

Supporting Information may be found in the online version of this article.

Correspondence to:

S. Zhong,
szhong@colorado.edu

Citation:

Zhong, S., Kang, K., A, G., & Qin, C. (2022). CitcomSVE: A three-dimensional finite element software package for modeling planetary mantle's viscoelastic deformation in response to surface and tidal loads. *Geochemistry, Geophysics, Geosystems*, *23*, e2022GC010359. https://doi.org/10.1029/2022GC010359

Received 24 JAN 2022
Accepted 26 MAY 2022

CitcomSVE: A Three-Dimensional Finite Element Software Package for Modeling Planetary Mantle's Viscoelastic Deformation in Response to Surface and Tidal Loads

Shijie Zhong[1], Kaixuan Kang[1], Geruo A[2], and Chuan Qin[1]

[1]Department of Physics, University of Colorado, Boulder, CO, USA, [2]Department of Earth Sciences, University of California at Irvine, Irvine, CA, USA

Abstract This article presents a comprehensive benchmark study for the newly updated and publicly available finite element code CitcomSVE for modeling dynamic deformation of a viscoelastic and incompressible planetary mantle in response to surface and tidal loading. A complete description of CitcomSVE's finite element formulation including calculations of the sea-level change, polar wander, apparent center of mass motion, and removal of mantle net rotation is presented. The 3-D displacements and displacement rates and the gravitational potential anomalies are solved with CitcomSVE for three benchmark problems using different spatial and temporal resolutions: (a) surface loading of single harmonics, (b) degree-2 tidal loading, and (c) the ICE-6G GIA model. The solutions are compared with semi-analytical solutions for error analyses. The benchmark calculations demonstrate the accuracy and efficiency of CitcomSVE. For example, for a typical ICE-6G GIA calculation with a 122-ky glaciation-deglaciation history, time increment of 100 years, and ~50 km (or ~0.5°) surface horizontal resolution, it takes ~4.5 hr on 96 CPU cores to complete with about 1% and 5% errors for displacements and displacement rates, respectively. Error analyses shows that CitcomSVE achieves a second order accuracy, but the errors are insensitive to temporal resolution. CitcomSVE achieves the parallel computational efficiency >75% for using up to 6,144 CPU cores on a parallel supercomputer. With its accuracy, computational efficiency and its open-source public availability, CitcomSVE provides a powerful tool for modeling viscoelastic deformation of a planetary mantle with 3-D mantle viscous and elastic structures in response to surface and tidal loading problems.

Plain Language Summary As high-quality geodetic observations of Earth's surface deformation and gravity anomalies in response to tidal and surface loads (e.g., deglaciation) become readily available, and as powerful parallel supercomputers are more accessible, modeling dynamic deformation of the Earth's mantle with realistic 3-D mantle viscoelastic rheology becomes both necessary and feasible. However, such modeling studies require an accurate, efficient and robust numerical modeling software package. This study presents a newly updated and publicly accessible finite element code CitcomSVE that can perform such modeling studies. This study describes the finite element formulation in CitcomSVE including calculations of other important geophysical processes such as sea level change, polar wander and apparent motion of Earth's center of mass. Three different benchmark calculations are performed at different spatial and temporal resolutions, and numerical errors are determined by comparing CitcomSVE solutions with semi-analytical solutions. The benchmark calculations demonstrate that CitcomSVE is highly accurate and efficient and can be applied for modeling glacial isostatic compensation and tidal loading problems.

1. Introduction

The deformational properties of a terrestrial planetary mantle including mantle elastic moduli and viscosity determine planetary deformation in response to forcings. A forcing can have vastly different sets of time-scales ranging from seconds as in seismic wave propagation (e.g., Dziewonski & Anderson, 1981) to a day as for tides (e.g., Longman, 1966). In addition, there are even longer relevant time scales such as months or years as for post-seismic deformation (e.g., Nur & Mavko, 1974), tens of thousands of years as for glacial isostatic adjustment (GIA) (e.g., Peltier, 1976),millions of years as for long-term tectonic and mantle dynamic forcing of volcanic building (e.g., Watts, 2001) and mantle convection (e.g., Schubert et al., 2001), and possibly billions of years of tidal-rotational forcing due to planetary orbit changes (e.g., Qin et al., 2018). Depending on the time-scale of a forcing, the mantle may respond differently and display purely elastic, viscoelastic, and purely viscous

deformations for short, intermediate and long time-scales, respectively. The deformational responses to a forcing are determined by solving the equations of motion with relevant rheological properties of the mantle.

With the assumption of spherical symmetry in elasticity and viscosity structure (i.e., only 1-D or radial dependence), the equations of motion can be solved analytically in spectral domains to determine the displacement, strain and stress of planetary mantles on different time scales (e.g., Dahlen & Tromp, 1998; Hager & O'Connell, 1981; Longman, 1966; Qin et al., 2018; Takeuchi, 1950; Wu & Peltier, 1982). For the mantle with fully 3-D elastic and viscosity structures, special solution techniques are required to solve the equations of motion. For example, perturbation methods have been used for seismic wave propagation (e.g., Dahlen & Tromp, 1998) and tidal deformation (e.g., Lau et al., 2017; Qin et al., 2014, 2016) problems for a planetary mantle with weak lateral variations in elastic properties. However, because mantle viscosity may vary by orders of magnitude due to its strong dependence on temperature, numerical methods are preferred for viscous flow (e.g., Zhong et al., 2007) and more specifically, for viscoelastic deformation, commonly used numerical methods include a spectral-finite element (e.g., Bagge et al., 2021; Klemann et al., 2008; Martinec, 2000), finite element (e.g., Hu & Wang, 2012; Zhong et al., 2003), finite volume (e.g., Latychev et al., 2005), and coupled spectral-finite element (Wu, 2004; van der Wal et al., 2013) methods.

The CitcomSVE package is a finite element modeling package for solving load-induced viscoelastic deformation problems in a 3-D spherical shell, a spherical wedge or Cartesian domain. CitcomSVE works for 3-D viscoelastic mantle structure with either linear or non-linear viscosity. It works efficiently on massively parallel computers (>6,000 CPU cores) with MPI for inter-CPU node communications. It has been developed over the last two decades to solve for dynamic deformation and response of a planetary mantle to three types of forcing or loads: (a) time-dependent loading on the surface of a viscoelastic mantle (e.g., GIA or volcanic loading) (Bellas et al., 2020; A et al., 2013; Paulson et al., 2005; Zhong & Watts, 2013; Zhong et al., 2003, 2012); (b) tidal forcing on a purely elastic mantle (e.g., tidal deformation) (Qin et al., 2014, 2016; Zhong et al., 2012); (c) long-term tidal-rotational forcing for a viscoelastic mantle (e.g., the planetary tidal-rotational bulge or figure) (Qin et al., 2018). CitcomSVE has been used for GIA studies for both the incompressible (Zhong et al., 2003) and compressible (A et al., 2013) mantle with temperature- (Paulson et al., 2005) and stress-dependent viscosity (Kang et al., 2022). CitcomSVE was built from mantle convection modeling package CitcomS (Zhong et al., 2000, 2008) by replacing viscous rheology and Eulerian formulation in CitcomS with viscoelastic rheology and Lagrangian formulation, respectively (Zhong et al., 2003).

This paper describes the physical models, mathematical structure and computational methods for CitcomSVE, and presents benchmark and error analysis studies for three distinct problems solved by CitcomSVE: surface loading of different single harmonics, tidal loading, and the ICE-6G GIA model (Peltier et al., 2015). For simplicity and benchmark purpose, this paper focuses on incompressible mantle models with an either homogeneous or 1-D (i.e., radially stratified) viscoelastic structure. For each type of the loading problems, example calculations using CitcomSVE will be presented and compared with semi-analytical solutions to verify the accuracy of CitcomSVE. Although our previous studies using CitcomSVE included some limited benchmark calculations (e.g., A et al., 2013; Paulson et al., 2005; Qin et al., 2014; Zhong et al., 2003), the current study differs from our previous studies in a number of important ways. First, the current study put together all the most relevant components of model formulations, numerical analysis and calculations of geophysical variables and process in CitcomSVE that were presented in different papers. Second, the current study introduces an updated and publicly available version of CitcomSVE that runs on thousands of CPU cores on massively parallel computers, while the earlier version of CitcomSVE used only 12 CPU cores. Third, this is a significantly more complete benchmark study with different spatial and temporal resolutions and detailed error analyses. Fourth, the current study reports not only accuracy but also computational speed and parallel computing efficiency for CitcomSVE. Although this study only considers CitcomSVE, it can be considered as continuation of GIA community's benchmark effort (Spada et al., 2011; Martinec et al., 2018). The paper is organized as follows. Next section or Section 2 is for governing equations for dynamic loading problems and numerical methods. Section 3 presents example model calculations for those three different loading problems and corresponding benchmark results. Discussions and conclusions are given in the final section.

Table 1
Model Parameters for Example, Calculations

Model parameters	Value
Earth radius r_s	6,370 km
CMB radius r_b	3,503.5 km
Mantle density ρ_0	4,604.4 kg/m^3
Density increase at CMB $\Delta\rho$	5,401 kg/m^3
Water density ρ_w	1,000 kg/m^3
Ice density ρ_i	917.4 kg/m^3
Shear modulus μ	1.4305×10^{11} Pa
Modified Fluid Love number $k_{2f}(1+\delta)$	1.11664
Mantle reference viscosity η	10^{21} Pa·s
Gravitational acceleration g	9.8 m · s^{-2}
VM5A viscosity model:	
The surface to 60 km depth	10^{26} Pas
60–100 km depth	10^{22} Pas
100–670 km depth	4.853×10^{21} Pas
670–1,170 km	1.5048×10^{21} Pas
1,170 km to CMB	3.095×10^{21} Pas

2. Governing Equations and Numerical Methods

2.1. Governing Equations and Boundary Conditions

The governing equations for load-induced deformation are derived from the laws of conservation of mass and momentum and Newton's law of gravitation. A simplified formulation with the assumption that the mantle is an incompressible medium is given as (e.g., Martinec, 2000; Wu, 2004; Wu & Peltier, 1982; Zhong et al., 2003):

$$u_{i,i} = 0, \tag{1}$$

$$\sigma_{ij,j} + \rho_0 \phi_{,i} - (\rho_0 g u_r)_{,i} - \rho_1^E g_i + \rho_0 V_{a,i} = 0, \tag{2}$$

$$\phi_{,ii} = -4\pi G \rho_1^E, \tag{3}$$

where u_i represents the displacement vector with u_r being in the radial direction, ϕ is the perturbation of gravitational potential due to deformation, V_a is the applied potential (e.g., rotational and tidal potentials) when applicable, σ_{ij} is the stress tensor, ρ_0 is the unperturbed mantle density, g_i is the gravitational acceleration with $g = \sqrt{g_i g_i}$, $\rho_1^E = -u_i \rho_{0,i}$ is the Eulerian density perturbation, and G is the gravitational constant. The equations are written in a indicial notation such that $A_{,i}$ represents the derivative of variable A with respect to coordinate x_i, and repeated indices indicate summation. CitcomSVE package has implemented formulations for both incompressible (e.g., Zhong et al., 2003) and compressible (A et al., 2013) medium. Here we only discuss CitcomSVE model formulation for incompressible medium in this paper.

Surface traction boundary conditions with zero shear force are applied at the surface (at radius $r = r_s$) and core-mantle boundary (CMB) ($r = r_b$) such that both the surface and CMB can deform dynamically in both horizontal and radial directions. The boundary conditions are

$$\sigma_{ij} n_j = -\sigma_o n_i, \quad \text{for } r = r_s, \tag{4}$$

$$\sigma_{ij} n_j = (-\rho_c \phi + \rho_c g u_r) n_i, \quad \text{for } r = r_b, \tag{5}$$

where σ_o represents the pressure loads at the surface (e.g., glacial loads) as a function of time and space, ρ_c is the density of the core, and n_i represents the normal vector of the surface or CMB. The boundary conditions at the CMB consider the self-gravitational effect for a fluid core (e.g., Zhong et al., 2003). ρ_c, together with mantle density ρ_m, is given in Table 1. Our models assume a constant gravitational acceleration g throughout the mantle (Table 1). Other than this CMB boundary condition, the core is not considered explicitly in our numerical formulation. Note that tidal or centrifugal forcing loads are applied via applied potential V (see Section 3.2.1), and surface loads $\sigma_o(t, \theta, \varphi)$ are zero.

The boundary conditions for Poisson's equation (i.e., Equation 3) are given by

$$\phi\left(r^+\right) = \phi\left(r^-\right), \quad \text{for } r = r_s \text{ and } r = r_b, \tag{6}$$

$$n_i \phi_{,i}\left(r^+\right) + 4\pi G \rho\left(r^+\right) n_i u_i\left(r^+\right) = n_i \phi_{,i}\left(r^-\right) + 4\pi G \rho\left(r^-\right) n_i u_i\left(r^-\right), \quad \text{for } r = r_s \text{ and } r = r_b, \tag{7}$$

where $\rho(r^+) = 0$ at the surface.

2.2. Rheological Equations

We consider a planetary mantle as an incompressible viscoelastic Maxwell solid for which the total deformation is the sum of elastics and viscous deformation. Elastic and viscous deformation can each be related to the stress tensor by

$$\varepsilon_{ij}^{e} = \frac{1}{2\mu}\left(\sigma_{ij} + P\delta_{ij}\right), \tag{8}$$

$$\dot{\varepsilon}_{ij}^{v} = \frac{1}{2\eta}(\sigma_{ij} + P\delta_{ij}), \tag{9}$$

where ε_{ij}^{e} and $\dot{\varepsilon}_{ij}^{v}$ are elastic strain tensor and viscous strain rate tensor, respectively, P is the dynamic pressure, δ_{ij} is the Kronecker delta function, and μ and η are the shear modulus and viscosity, respectively. The total strain ε_{ij} is the sum of elastic and viscous strains and can be related to displacement by

$$\varepsilon_{ij} = \varepsilon_{ij}^{e} + \varepsilon_{ij}^{v} = \frac{1}{2}\left(\frac{\partial u_i}{\partial x_j} + \frac{\partial u_j}{\partial x_i}\right) \tag{10}$$

Adding time derivative of Equations 8 and 9 leads to the following rheological equation,

$$\sigma_{ij} + \frac{\eta}{\mu}\dot{\sigma}_{ij} = -\left(P + \frac{\eta}{\mu}\dot{P}\right)\delta_{ij} + 2\eta\dot{\varepsilon}_{ij}, \tag{11}$$

where the dot over a variable represents time-derivative.

Both shear modulus μ and viscosity η can be fully three-dimensional in CitcomSVE models to represent the effects of temperature and composition on mantle mechanical properties (e.g., A et al., 2013; Paulson et al., 2005; Zhong et al., 2003). Other rheological equations representing realistic deformation mechanisms including frictional sliding, low-temperature plasticity and power-law creep have also been implemented in CitcomSVE (e.g., Bellas et al., 2020; Kang et al., 2022; Zhong & Watts, 2013). However, here for benchmark we will restrict our discussion to relatively simple rheological properties with uniform μ and either uniform or radially layered η.

It is important to point out that the Burgers model of viscoelasticity shows transient rheological effects (e.g., Lau & Faul, 2019) that are important for understanding short-term GIA (e.g., Ivins et al., 2022) and post-seismic deformation processes (e.g., Hetland & Hager, 2005; Hu & Wang, 2012). However, the Burgers rheology has not been used in numerical GIA models, although it has been implemented for post-seismic deformation (e.g., Hu & Wang, 2012).

2.3. Numerical Formulation and Analysis

A finite element method is used in CitcomSVE package to solve Equations 1 and 2 for load-induced displacement and stress under boundary conditions Equations 4 and 5 with a Maxwell rheological Equation 11. Equation 3 for gravitational potential with boundary conditions Equations 6 and 7 is solved using a spherical harmonic spectral method. For full descriptions of finite element analysis and spectral method, see Zhong et al. (2003) and A et al. (2013) for models of incompressible and compressible medium, respectively. Here we will present some key aspects of the numerical methods for incompressible medium. We will describe methods for modeling geophysical processes including polar wander and degree-1 displacement in CitcomSVE (A et al., 2013; Paulson et al., 2005).

2.3.1. Incremental Displacement Formulation and Discretized Rheological Equation

Although governing Equations 1–3 do not contain any time-dependent terms as they describe static equilibria, time-dependence occurs in Maxwell viscoelastic rheological Equation 11. We employ an incremental displacement formulation for the time-dependent deformation problems (Zhong et al., 2003). Let u_i^n and u_i^{n-1} be displacements at times t and $t - \Delta t$, respectively, where superscripts n and $n - 1$ represent time steps for corresponding times. Incremental displacement at time t is defined as $v_i^n = u_i^n - u_i^{n-1}$ and it can be used to define incremental strain as

$$\Delta\varepsilon_{ij}^{n} = \frac{1}{2}\left(\frac{\partial v_i^n}{\partial x_j} + \frac{\partial v_j^n}{\partial x_i}\right). \tag{12}$$

Rheological Equation 11 is discretized in time by integrating it from time $t-\Delta t$ to t, and stress tensor at time t, σ_{ij}^n, is recast in terms of incremental strain $\Delta\varepsilon_{ij}^n$ and pre-stress τ_{ij}^{pre} as (Zhong et al., 2003),

$$\sigma_{ij}^n = -P^n\delta_{ij} + 2\tilde{\eta}\Delta\varepsilon_{ij}^n + f\tau_{ij}^{\text{pre}}, \tag{13}$$

where $\tilde{\eta} = \eta/(\alpha+\Delta t)$, $f = (\alpha-\Delta t/2)/(\alpha+\Delta t/2)$, $\tau_{ij}^{\text{pre}} = \sigma_{ij}^{n-1} + P^{n-1}\delta_{ij}$, and $\alpha = \eta/\mu$ (i.e., the Maxwell time). Note that the pre-stress is the deviatoric stress at timestep $n-1$, $\tau_{ij}^{\text{pre}} = \tau_{ij}^{n-1}$, given that the deviatoric stress is $\tau_{ij} = \sigma_{ij} + P\delta_{ij}$. Equation 13, the discretized rheological equation, with the pre-stress term, is similar to that in Martinec (2000) who applied a finite difference scheme to the time derivative term in the rheological equation.

2.3.2. Solution of Poisson's Equation for Gravitational Potential

Poisson's equation for gravitational potential anomaly ϕ is solved in spherical harmonic domain (see the definition of spherical harmonics and harmonic expansion used in CitcomSVE in Section 2.4.5 and also in Zhong et al., 2003, 2008). All the relevant variables at time t are expressed in terms of spherical harmonic degree l and order m, for example, gravitational potential anomaly at radius r and time t as $\phi_{lm}(r,t)$. Under the incompressibility approximation, three sources of mass anomalies may contribute to $\phi_{lm}(r,t)$: surface topography (i.e., radial displacement) $u_{lm}^s(t)$, CMB topography $u_{lm}^b(t)$, and the surface loads $\sigma_{0\_lm}(t)$.

$$\phi_{lm}(r,t) = \frac{4\pi G}{2l+1}\left\{ r_b\left(\frac{r_b}{r}\right)^{l+1}\Delta\rho_b u_{lm}^b(t) + r_s\left(\frac{r}{r_s}\right)^{l}\left[\Delta\rho_s u_{lm}^s(t) + \frac{\sigma_{0\_lm}(t)}{g}\right]\right\}, \tag{14}$$

where $\Delta\rho_b$ and $\Delta\rho_s$ are density differences across the CMB and surface, respectively.

Using the incremental formulation, let $v_{lm}^b(t) = u_{lm}^b(t) - u_{lm}^b(t-\Delta t)$, $v_{lm}^s(t) = u_{lm}^s(t) - u_{lm}^s(t-\Delta t)$, and $\Delta\sigma_{0\_lm}(t) = \sigma_{0\_lm}(t) - \sigma_{0\_lm}(t-\Delta t)$ be the incremental radial CMB and surface displacements and incremental loads, respectively, and incremental potential $\Delta\phi_{lm}(r,t)$ is given as

$$\phi_{lm}(r,t) = \phi_{lm}(r,t-\Delta t) + \Delta\phi_{lm}(r,t), \tag{15}$$

where $\phi_{lm}(r,t-\Delta t) = \Phi_{lm}(r)$ is the potential at the previous time step and can be viewed as a known quantity, and $\Delta\phi_{lm}(r,t)$ is related to the unknown incremental displacements $v_{lm}^b(t)$ and $v_{lm}^s(t)$ as

$$\Delta\phi_{lm}(r,t) = \frac{4\pi G}{2l+1}\left\{ r_b\left(\frac{r_b}{r}\right)^{l+1}\Delta\rho_b v_{lm}^b(t) + r_s\left(\frac{r}{r_s}\right)^{l}\left[\Delta\rho_s v_{lm}^s(t) + \frac{\Delta\sigma_{0\_lm}(t)}{g}\right]\right\}. \tag{16}$$

2.3.3. Finite Element Analysis and Solution Methods

Applying the weak form of finite element formulation to the equation of motion (i.e., Equation 2) (Hughes, 2000; Zhong et al., 2003) leads to

$$\begin{aligned}
&\int_\Omega w_{i,j}\left[-\tilde{P}\delta_{ij} + \tilde{\eta}\left(v_{i,j}+v_{j,i}\right)\right]\mathrm{d}V + \int_S w_i\Delta\rho_s g v_r\delta_{ir}\mathrm{d}S + \int_B w_i\Delta\rho_b g v_r\delta_{ir}\mathrm{d}S \\
&= -\int_\Omega w_{i,j} f\tau_{ij}^{\text{pre}}\mathrm{d}V + \int_S w_i\left(\rho_0 V_a + \rho_0\Phi - \Delta\rho_s g U_{rs} - \sigma_0\right)\delta_{ir}\mathrm{d}S \\
&+ \int_B w_i\Delta\rho_b\left(\Phi + V_a - gU_{rb}\right)\delta_{ir}\mathrm{d}S + \int_S w_i\rho_0\Delta\phi\delta_{ir}\mathrm{d}S + \int_B w_i\Delta\rho_b\Delta\phi\delta_{ir}\mathrm{d}S,
\end{aligned} \tag{17}$$

where integration domain Ω, S, and B are for the volume, the surface and CMB boundaries, respectively, w_i is the displacement weighting function, $\tilde{P} = P - \rho_0\phi + \rho_0 g u_r$ is the effective pressure, and Φ, U_{rs} and U_{rb} are the potential, surface and CMB radial displacements at previous time step, respectively.

Equation 17 and the conservation equation of the mass (i.e., Equation 1) are discretized onto a set of finite element grid to form a system of matrix equations with unknown vectors of the effective pressure $\{P\}$ and incremental displacement $\{V\}$.

$$\left[A^T\right]\{V\} = \{0\}, \tag{18}$$

$$([K]+[B])\{V\} + [A]\{P\} = \{F_0\} + \{F\}, \tag{19}$$

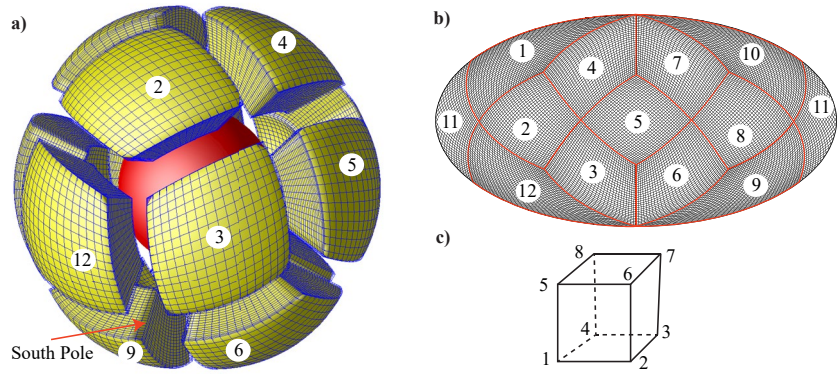

Figure 1. A 3-D view (a) and mapview (b) of the finite element grid with 12 spherical caps covering a spherical shell, and an eight-node trilinear element (c) used in CitcomSVE. Each of the 12 caps in Figures 1a and 1b includes a certain number of finite elements in the radial direction and two azimuthal directions, and each cap can also be further divided into smaller blocks for a parallel computing purpose. The thick red lines in Figure 1b mark the shared boundaries of the 12 caps. In Figure 1a, the caps are separated for a better view. The numbers in Figures 1a and 1b show the ordering of the 12 caps. The numbers in Figure 1c show the ordering of local nodes of the element. Figures 1a and 1b are modified from Zhong et al. (2000).

where $[A]$ is the gradient matrix, $\left[A^T\right]$ is the transpose of $[A]$, $[K]$ is the stiffness matrix, $[B]$ is a boundary matrix that is derived from the second and third integrals on the left hand side of Equation 17, $\{F_0\}$ is the force vector representing contributions from the previous time step (i.e., the first three integrals of the right hand side of Equation 17), and $\{F\}$ represents contributions from the current time step (i.e., the last two terms of the right hand side of Equation 17). Note that $\{F\}$ depends on unknown displacements at the surface and CMB.

CitcomSVE code has been developed out of 3-D finite element code CitcomS for mantle convection in a spherical shell, and they share many common features. The spherical shell of the mantle is divided into 12 caps of similar size, and each cap is further divided into a grid of cells (i.e., elements) of similar size (Figures 1a and 1b) (Zhong et al., 2000, 2008). Following Citcom (Moresi & Solomatov, 1995; Moresi et al., 1996), CitcomSVE uses brick elements with eight displacement nodes and one central pressure node per element (Figure 1c). This design of finite element grid is suited for parallel computing, as discussed in Zhong et al. (2008). Another important feature of this grid is its approximately uniform resolution from the polar to equatorial regions (Zhong et al., 2000, 2003). This is different from the spectral finite element code by Martinec and his colleagues (Bagge et al., 2021; Klemann et al., 2008; Martinec, 2000) that uses spherical harmonic representation for azimuthal variations and the coupled-spectral finite element code by Wu and his colleagues (Li et al., 2020; van der Wal et al., 2013; Wu, 2004) with a grid of constant increment in longitude and latitude directions (e.g., $1^\circ \times 1^\circ$), both of which may lead to excessively high resolution in the polar region than that in equatorial region.

Matrix Equations 18 and 19 are solved with the Uzawa algorithm coupled with the full multigrid method (Moresi & Solomatov, 1995; Zhong et al., 2000, 2008). The general solution strategy in CitcomSVE follows an iterative scheme that can be summarized by (Zhong et al., 2003):

1. At a given time t, $\{F_0\}$ is first evaluated using deviatoric stress τ_{ij}^{pre}, gravitational potential Φ, and radial displacements at the surface and CMB, U_{rs} and U_{rb}, at the previous time step, $t - \Delta t$, and set $\{F\} = \{0\}$.
2. Solve Equations 18 and 19 for incremental displacements $\{V\}$ and effective pressure $\{P\}$, using $\{F_0\}$ and $\{F\}$.
3. Compute incremental potential $\Delta\phi_{lm}(r,t)$ using Equation 16 with the incremental radial displacements at the surface and CMB from step 2, and then re-evaluate $\{F\}$. Go back to step 2 to solve for $\{V\}$ and $\{P\}$ again.
4. Repeat steps 2 and 3, until $\{V\}$ and $\{P\}$ converge to a given threshold error tolerance. Then go back to step 1 to march forward in time.

It is helpful to point out that in step 3 the potential is computed in the spherical harmonic domain for each harmonics l and m, but the displacement $\{V\}$ that is needed for computing the potential is solved on the finite element grid of CitcomSVE. Therefore, the radial displacements at the surface and CMB must be transformed from the grid to the spherical harmonic domain via the spherical harmonic expansion in order to compute the

potential using Equation 16 (Zhong et al., 2003). In computing $\{F\}$ using the potential, the potential needs to be recast to the grid from the spherical harmonic domain. These forward and inverse spherical harmonic expansion operations can be computationally expensive, if a large number of harmonics are involved, partly because the finite element grid (Figures 1a and 1b) is a non-Gauss-Legendre grid.

2.4. Calculations of Geophysical Processes and Variables in CitcomSVE

Loading on planetary surface may lead to certain geophysical processes including polar wander, apparent motion of the center of mass (i.e., degree-1 deformation), net rotation of the mantle, sea-level change (when mass exchange between continental ice mass and oceans is present). Here we discuss calculations of these geophysical processes and quantities in CitcomSVE.

2.4.1. Degree-1 Deformation–Apparent Motion of Center of Mass

The center of mass here refers to the center of the Earth-load system. In the absence of external force, the center of mass is fixed (excluding the Earth's orbital motion and its associated forces) and should be used as the reference frame with which the displacement is measured (e.g., via satellites). In the loading formulation presented here, surface loads such as those associated with glacial and melt-water mass are considered as external to the solid Earth. The load distribution can have a hemispherically asymmetric structure (i.e., spherical harmonic degree 1), thus causing degree-1 displacement for the solid Earth. The degree-1 displacement can also occur when the mantle has lateral variations in elastic or/and viscosity structures. However, the loading formulation computes displacements in the model frame (i.e., relative to the coordinates of the numerical model) and does not guarantee that the degree-1 displacement is relative to the center of mass. Therefore, it is necessary to process the model results such that they are relative to the center of mass, as done in Paulson et al. (2005) and A et al. (2013) for CitcomSVE for incompressible and compressible models, respectively.

The calculation of degree-1 displacement consists of the following steps (Paulson et al., 2005; A et al., 2013). (a) Calculate the center of mass of the Earth-load system relative to the model frame, $\boldsymbol{r}_{\mathrm{cm}}$, at the beginning of each time step using the incremental loads (e.g., ice and water distribution) for this time step and solid Earth's incremental displacements at density interfaces (e.g., the surface and CMB) from the previous time step. (b) Shift the incremental displacements by $\boldsymbol{r}_{\mathrm{cm}}$ for a translation to the center of mass frame. This corresponds to modifying the loads by adding $-\Delta\rho g r_{\mathrm{cm}} \cos\vartheta$ to the loads for each density interface such that they are relative to the center of mass frame, where $\Delta\rho$ is the density difference across the density interface and ϑ is the angle between $\boldsymbol{r}_{\mathrm{cm}}$ and the position vector at a point on the density boundary. This step causes the degree-1 gravitational potential to vanish. (c) Solve the governing equations for the incremental displacement using the updated loads for the current time step. The new incremental displacements at density boundaries will in general cause the center of mass motion to shift its position. We repeat step a) to determine $\boldsymbol{r}_{\mathrm{cm}}$ and perform a translation to the new center of mass frame, leading to updated incremental displacements for the current time step.

Three remarks are warranted here. (a) The translation operation between the model frame and the center of mass frame does not affect stress calculations which can be conveniently done in the model frame. (b) Since the iterative solution method is used to solve Equations 18 and 19 for incremental displacements for each time step (see Section 2.3.3), the translation operation between these two frames is done for each iteration such that Equations 18 and 19 are always solved in the center of mass frame. (c) Step a) in determining $\boldsymbol{r}_{\mathrm{cm}}$ can also be done by computing degree-1 gravitational potential first and then solving $\boldsymbol{r}_{\mathrm{cm}}$ such that the degree-1 gravitational potential vanishes. We found that both methods for determining $\boldsymbol{r}_{\mathrm{cm}}$ are equivalent.

2.4.2. Removal of Mantle Pure Rotation

The loading that is considered in this study is either in the radial direction along the force of gravity (e.g., glacial loads) or symmetric (e.g., tidal or rotational forcing), suggesting that the loading does not induce pure rotation motion for the planet. However, numerical solutions of the conservation equation of momentum (i.e., Equation 2) may contain spurious pure rotation motion of the whole planet, because the pure rotation motion is unconstrained by the conservation equations (i.e., adding an arbitrary pure rotation motion does not affect the governing equations). While such pure rotation motion does not affect the dynamics or radial displacement, it is important to

remove this rotation motion such that displacements are in no rotation mantle frame. Here we describe a scheme to remove pure rotation motion in CitcomSVE that has been used in our previous studies (A et al., 2013; Qin et al., 2016).

For the spherical shell of the mantle with inner radius r_b and outer radius r_s and a uniform density ρ_0 (i.e., for an incompressible medium), define $\boldsymbol{v}$ as incremental displacement vector, $\boldsymbol{r}$ as position vector, and $\boldsymbol{\alpha}$ as the incremental angular displacement vector of the pure rotation of the whole mantle, then considering the definition of the angular momentum of the mantle and the moment of inertia of the mantle $I = 8\pi\rho_0\left(r_s^5 - r_b^5\right)/15$, the following equation must hold (Zhong et al., 2008),

$$\boldsymbol{\alpha} = \frac{15}{8\pi\left(r_s^5 - r_b^5\right)} \int \boldsymbol{r} \times \boldsymbol{v} \mathrm{d}V, \tag{20}$$

where the integration is for the whole mantle. Removing the displacement associated with this pure rotational motion of the mantle from the original displacement $\boldsymbol{v}$ leads to the revised displacement $\tilde{\boldsymbol{v}}$ in the no rotation frame of the mantle:

$$\tilde{\boldsymbol{v}} = \boldsymbol{v} - (\boldsymbol{r} \times \boldsymbol{\alpha}). \tag{21}$$

It should be pointed out that a similar scheme is used in mantle convection code CitcomS to remove the pure rotation of the mantle (Zhong, 2001; Zhong et al., 2008), which is important for mantle dynamics (e.g., Becker, 2006). Although the scheme presented here is for an incompressible medium, extending it for a compressible mantle with a depth-dependent density structure is straightforward (see Section 2.6) (A et al., 2013; Tan et al., 2011).

2.4.3. Sea Level Change and Sea Level Equation

One of the applications of the CitcomSVE package has been on modeling the GIA process (e.g., A et al., 2013; Paulson et al., 2005, 2007; Zhong et al., 2003). For GIA problems, it is essential to consider mass exchange and redistribution between ice on continents and water in oceans. As the ice melts, the water goes to oceans, causing sea level rise globally. Because sea level follows an equipotential surface or the geoid which is affected by mass anomalies associated with variations of ocean water and ice and with incremental radial displacements at the surface and CMB (or any other density interfaces in the mantle), it is important to couple these processes together to determine how the melt water is distributed into oceans. Here we summarize how the sea level equation (Farrell & Clark, 1976) is implemented in CitcomSVE to determine melt water mass distribution and sea level change (A et al., 2013; Paulson et al., 2005).

The change in height of ocean load, L_0, since the onset of glaciation is determined by the sea level equation (Farrell & Clark, 1976)

$$L_0(\theta, \varphi, t) = [N(\theta, \varphi, t) - U(\theta, \varphi, t) + c(t)]O(\theta, \varphi, t), \tag{22}$$

where N and U are the GIA-related geoid anomalies (i.e., equipotential surface variation) and radial displacements at the surface, O is the ocean function (1 for ocean and 0 elsewhere), and c is the barystatic sea level as

$$c(t) = \frac{1}{A_0}\left[-\frac{M_{\mathrm{ice}}(t)}{\rho_w} - \int (N - U)O \mathrm{d}S\right], \tag{23}$$

where A_0 is the area of the oceans, ρ_w is the density of water, $M_{\mathrm{ice}}(t)$ is the ice mass, and the integral is for the surface of the Earth. $M_{\mathrm{ice}}(t)$ is calculated for a given ice history model, for example, ICE-6G (Peltier et al., 2015). Ocean function O which is time-dependent can be constructed from present-day ocean-continent distribution and ice history model.

The ocean load (i.e., the change of ocean height) depends on incremental displacement and geoid (Equation 22), and also affects them via the equation of motion and Poisson's equation for gravitational potential. The iterative solution method as discussed in Section 2.3.3 solves for displacements, and gravitational potential and sea level height changes self-consistently. Due to improved computational efficiency in CitcomSVE, the iterative scheme is applied for every timestep, different from an earlier version of CitcomSVE where the iterations were only applied for the first few timesteps and were subsequently replaced by extrapolations (Paulson et al., 2005; Zhong et al., 2003). As discussed in A et al. (2013), our sea level calculations consider the dynamic effects

of Earth's geoid, rotational potential and radial displacement, and the calculations also consider a prescribed, time-dependent ocean-continent function that includes the effect of ice melting that turns the land to ocean regions (e.g., the Hudson Bay). However, our sea level calculations ignore the effects of moving shorelines for a given time step and sloping bathymetry (e.g., Kendall et al., 2005; Milne, 1998).

2.4.4. Polar Wander

Any mass change at the surface and in the interiors of a planet may cause planetary moment of inertia to change, thus perturbing planetary rotation vector and causing polar motion. This phenomenon happens on geological time scales of hundreds of millions of years (i.e., true polar wander) and also on relatively short time scales for processes like GIA. For the GIA process, polar wander induces perturbation to Earth's centrifugal potential that in turn affects the deformation of the Earth's mantle (e.g., Mitrovica et al., 2005). The effect of polar wander in the GIA process has been incorporated in CitcomSVE models (A et al., 2013; Paulson et al., 2005). Here we summarize key concept of polar wander calculations and its implementation in CitcomSVE.

Define the Earth's rotational angular velocity $\boldsymbol{\omega} = \Omega\,(m_x, m_y, 1 + m_z)$, where Ω is the unperturbed rotational rate, and m_x, m_y and m_z represent the perturbations in each of three directions. Using complex number notation, define $m_\pm = m_x \pm i m_y$, and $I_\pm = I_{xz} \pm i I_{yz}$, where I_{xz} and I_{yz} are the perturbed moment of inertia due to GIA process. Then for periods longer than the Chandler wobble, these perturbed quantities can be related to each other by (Lambeck, 1980; Paulson et al., 2005),

$$m_\pm = \frac{I_\pm}{(C - A)_{\text{hyd}}(1 + \delta)} \tag{24}$$

where C and A are the unperturbed principal polar and equatorial moments of inertia, δ describes the long-term non-hydrostatic oblateness (i.e., $\delta \sim 0.8\%$ (Mitrovica et al., 2005; Paulson et al., 2005)), and $(C{-}A)_{\text{hyd}}$ represents purely hydrostatic oblateness in response to rotation (e.g., Mitrovica et al., 2005):

$$(C - A)_{\text{hyd}} = \frac{r_o^5 \Omega^2 k_{2f}}{3G}, \tag{25}$$

where k_{2f} is the fluid Love number at degree 2. In this study, $k_{2f}(1 + \delta)$ is set to be 1.11664.

A consequence of polar wander is to introduce perturbations to centrifugal potential at spherical harmonic degree $l = 2$ and order $m = \pm 1$ as (Lambeck, 1980; Paulson et al., 2005)

$$\Delta\phi_c = \sqrt{\frac{2\pi}{15}}\Omega^2 r^2 \left(m_- Y_2^1(\theta, \varphi) - m_+ Y_2^{-1}(\theta, \varphi)\right), \tag{26}$$

where Y_2^1 and Y_2^{-1} are the spherical harmonic functions at $l = 2$ and $m = \pm 1$ in a complex form (e.g., Dahlen & Tromp, 1998) that are used here only for analysis purpose. Substituting Equation 24 to Equation 26 leads to

$$\Delta\phi_c = -\frac{\Omega^2 r^2}{(C - A)_{\text{hyd}}(1 + \delta)} \sin\theta \cos\theta \left(I_{xz} \cos\varphi + I_{yz} \sin\varphi\right), \tag{27}$$

which is a real function and is used in CitcomSVE calculations.

In CitcomSVE, at the beginning of each time step, mass anomalies due to loads at the surface (e.g., ice, melt water, and surface radial displacements) and in the mantle interiors (e.g., displacements at the CMB) are used to compute I_{xz}, I_{yz}, and the perturbed potential $\Delta\phi_c$ from Equation 27. $\Delta\phi_c$ is added to the gravitational potential anomalies in Equation 16 before the total potential is used in Equations 18 and 19 to solve for displacements. Since the displacements affect mass anomalies and hence I_{xz}, I_{yz}, and $\Delta\phi_c$, iterations are required to assure self-consistency. CitcomSVE uses the same iterative scheme and calculations as those for the calculations of the center of mass motion and sea level change for the polar wander calculations.

2.4.5. Calculations of Other Geophysical Variables

Stress tensor σ_{ij} at any given time step n can be computed in principle from Equation 13 after incremental displacement $\{V\}$ and effective pressure $\{P\}$ are solved from matrix Equations 18 and 19. However, it is troublesome to

calculate dynamic pressure P from the effective pressure $\{P\}$. Fortunately, in most cases only the deviatoric stress τ_{ij} is needed, and can be computed by re-arranging Equation 13 into

$$\tau_{ij}^{n} = \sigma_{ij}^{n} + P^{n}\delta_{ij} = 2\tilde{\eta}\Delta\varepsilon_{ij}^{n} + f\tau_{ij}^{\text{pre}}. \tag{28}$$

The deviatoric stress τ_{ij} is used as the pre-stress for calculations for the next time step. τ_{ij} is also used for other geophysical applications including stress-dependent viscosity modeling (Bellas & Zhong, 2021; Kang et al., 2022; Zhong & Watts, 2013) and GIA induced seismicity (e.g., Rollins et al., 2021). In fact, the total stress σ_{ij} is never computed in CitcomSVE.

As discussed at the end of Section 2.3.3, forward and inverse spherical harmonic expansion calculations are done frequently in solving the gravitational potential and incremental displacements between the finite element grid and the spherical harmonic domain. Following CitcomS, CitcomSVE uses a normalized associated Legendre polynomial p_{lm} as the basis function for spherical harmonic expansion (see Zhong et al., 2008). The normalized associated Legendre polynomial p_{lm} is related to the associated Legendre polynomial P_{lm} as:

$$p_{lm}(\theta) = \sqrt{\frac{(2l+1)(l-m)!}{2\pi\,(1+\delta_{m0})\,(l+m)!}}\,P_{lm}(\theta). \tag{29}$$

The spherical harmonic expansion of a scalar field, for example, radial displacement at the surface, $v^{s}(\theta,\varphi)$ is

$$v^{s}(\theta,\varphi) = \sum_{l=1}^{L}\sum_{m=0}^{l}\left[v_{lm}^{s\_c}\cos(m\varphi) + v_{lm}^{s\_s}\sin(m\varphi)\right]p_{lm}(\theta), \tag{30}$$

where $v_{lm}^{s\_c}$ and $v_{lm}^{s\_s}$ are the cosine and sine coefficients of the expansion that are used in Equation 16 for computing corresponding gravitational potential $\Delta\phi_{lm}$. Note that CitcomS/CitcomSVE uses real form spherical harmonic functions as in Equation 30 for computations (e.g., for gravitational potential or spherical harmonic expansion). Spherical harmonic expansion coefficients (e.g., in Equation 30) are computed in CitcomSVE by directly evaluating the relevant surface integrals on the finite element grid (Figure 1b).

2.5. Normalization in CitcomSVE

The calculations in CitcomSVE including output are done on non-dimensional variables. CitcomSVE uses the following normalization scheme. The coordinates x_i and displacements u_i and v_i are all normalized by radius of a planet, r_s, such that the normalized outer radius of the planet is 1. The time is normalized by the reference mantle Maxwell time $\alpha = \eta_r/\mu_r$, where η_r and μ_r are the reference mantle viscosity and shear modulus, respectively. $\eta_r$and μ_r are also used to normalize mantle viscosity and shear modulus, respectively, while the density is normalized by reference density ρ_0. The choice of these reference values is arbitrary, but they are typically those for the lower mantle. The stress tensor and pressure are normalized by reference shear modulus μ_r. Gravitational potential and centrifugal potential are normalized by $4\pi G\rho_0 r_s^2$, and the geoid anomalies are normalized by $4\pi G\rho_0 r_s^2/g$. Any other variables can be normalized by a combination of the above-mentioned scales.

2.6. Incompressible and Compressible Models in CitcomSVE

A et al. (2013) incorporated mantle compressibility into an early version of CitcomSVE that works for 12 CPU cores, and our near-term goal is to port the relevant codes for mantle compressibility that A et al. (2013) developed to the newly upgraded CitcomSVE that works on massively parallel computers. Based on our experience with its development and benchmark, we expect that CitcomSVE with mantle compressibility will have similar performance in both accuracy and computational efficiency, compared to the current code for an incompressible mantle. Mantle compressibility introduces two key differences. First, the mantle density is no longer homogeneous and is depth-dependent with jumps and continuous increase with depth, as in PREM (Dziewonski & Anderson, 1981). Second, the pressure term in the rheological Equation 11 will be replaced with bulk modulus, while the conservative equation of mass, that is, Equation 1, is no longer needed.

The depth-dependent density structure makes calculations more expensive relative to the incompressible model, although calculation procedures (i.e., the codes) remain similar. For example, in the calculations of gravitational potential, Equation 14 will need to include contributions from all the depths throughout the mantle, and so do the calculations of polar wander (i.e., for I_{xz} and I_{yz}), CM's apparent motion, and removal of pure rotational motion (A et al., 2013). The eliminations of the mass conservation equation and the pressure cause Equation 18 and the pressure term in Equation 19 to disappear, leading to a simpler matrix equation that can be solved with the full multi-grid solver directly for displacement vector $\{V\}$ without the need for the Uzawa algorithm (A et al., 2013). In short, we expect that CitcomSVE for compressible mantle will have similar performance to the current CitcomSVE for incompressible mantle.

3. Example Calculations and Benchmark Results

Three example problems that are solved using CitcomSVE are presented here. They are: (a) loading in a single spherical harmonic in space and step-function (i.e., Heaviside function) in time; (b) degree-2 tidal loading; and (c) GIA using ICE-6G ice history model. For each of the example problems, the elastic and viscosity structures are chosen to be simple: either homogeneous or only dependent on radius (i.e., 1-D), so that CitcomSVE solutions can be benchmarked against semi-analytical solutions.

3.1. Surface Loading in a Single Spherical Harmonic in Space and Step-Function in Time

3.1.1. Definition of the Surface Loading Problem

For the first example problem, we consider a surface load σ_0 (see Equation 4) corresponding to amplitude of topographic variation d with mantle material of density ρ_0 at a single harmonic function in space and step-function in time:

$$\sigma_0(t,\theta,\varphi) = \rho_0 g d \cos(m\varphi) p_{lm}(\theta) H(t) = \rho_0 g d \overline{P}_{lm}(\theta,\varphi) H(t), \tag{31}$$

where $H(t)$ is the Heaviside function (i.e., $H(t) = 1$ for $t \geq 0$; $H(t) = 0$ otherwise) and $\overline{P}_{lm}(\theta,\varphi) = \cos(m\varphi) p_{lm}(\theta)$ is the cosine part of spherical harmonic function in the real form. Note that for simplicity, only the cosine term of longitudinal dependence is considered. Normalizing the load by $\rho_0 g r_s$ leads to a dimensionless load with dimensionless amplitude of the load height $\delta = d/r_s$. δ is set to be small (10^{-6}) to avoid too large deformation of the grid. For this example, we assume an ocean-free Earth and ignore any sea-level related calculations. Model parameters used for incompressible Earth's mantle in our calculation are given in Table 1. This example problem has been used to benchmark the original version of CitcomSVE in Zhong et al. (2003) and A et al. (2013) for incompressible and compressible mantle, respectively. Here we compute time-dependent 3-D displacements in the mantle and gravitational potential anomalies in response to the applied load (i.e., Equation 31) using the newly updated CitcomSVE and compare the numerical model results with those from semi-analytical solutions (A et al., 2013; Han & Wahr, 1995; Paulson et al., 2005).

Compared with our previous benchmark calculations (e.g., A et al., 2013; Paulson et al., 2005; Zhong et al., 2003), this study includes three new features. First, the results are presented in terms of load Love numbers h_l, k_l, and l_l at harmonic degree l for radial displacement, gravitational potential, and horizontal displacement, respectively. Second, horizontal displacement is systematically investigated. Third, results of different numerical resolutions are used to determine the order of accuracy of CitcomSVE.

3.1.2. Calculations of Load Love Numbers From Numerical Models

Love numbers are generally defined as planetary responses in surface displacements and gravitational potential anomaly to an applied potential (e.g., tidal potential) (e.g., Lambeck, 1980; Spada et al., 2011). For example, for an applied potential $V_{0\_l}(\theta,\varphi)$ at spherical harmonic degree l where subscribe 0 indicates a given or applied potential, Love numbers h_l, k_l, and l_l are generally defined through the following equations for radial and horizontal displacements, u_r, u_θ, and u_φ, and gravitational potential ϕ:

$$u_r = h_l \frac{V_{0\_l}}{g}, \tag{32}$$

$$\phi = k_l V_{0\_l}, \tag{33}$$

$$u_\theta = \frac{l_l}{g}\frac{\partial V_{0\_l}}{\partial \theta}, \quad u_\varphi = \frac{l_l}{g\sin\theta}\frac{\partial V_{0\_l}}{\partial \varphi}. \tag{34}$$

If the applied potential is tidal potential, then such defined Love numbers are tidal Love numbers. For a planet with spherically symmetric structure (i.e., the structure only depends on radial coordinate r), the Love numbers are only dependent on l but not m and can be determined analytically using various techniques (e.g., Han & Wahr, 1995; Lambeck, 1980; Wu & Peltier, 1982; Zhong & Zuber, 2000).

The load Love numbers can be defined similarly by converting an applied surface load σ_0 to an equivalent gravitational potential that can then be treated as an applied potential. Using Equation 14, the applied surface load σ_0 (i.e., at $r = r_s$) in Equation 31 leads to gravitational potential at the surface for $t \geq 0$,

$$V_{0\_lm}(\theta, \varphi) = \frac{4\pi G}{2l+1}\rho_0 d r_s \overline{P}_{lm}(\theta, \varphi). \tag{35}$$

The radial displacement at the surface in response to the load can be written as

$$u_r(t, \theta, \varphi) = h_l(t)\frac{V_{0\_lm}(\theta, \varphi)}{g} = h_l(t)\frac{4\pi G}{(2l+1)g}\rho_0 \mathrm{d} r_s \overline{P}_{lm}(\theta, \varphi). \tag{36}$$

The time-dependence in $u_r(t, \theta, \varphi)$ arises from mantle viscoelastic relaxation, and radial displacement load Love number $h_l(t)$ is necessarily also time-dependent. Applying spherical harmonic expansion to $u_r(t, \theta, \varphi)$ (e.g., Equation 30) and considering $u_{rlm}(t)$ as the expansion coefficient for (l, m) (i.e., at the same harmonic as the load), Equation 36 leads to

$$h_l(t) = \frac{(2l+1)g}{4\pi G\rho_0 r_s}\frac{u_{rlm}(t)}{d} = \frac{(2l+1)g}{4\pi G\rho_0 r_s}\frac{u'_{rlm}(t)}{\delta}, \tag{37}$$

where $u'_{rlm}(t)$ and δ are dimensionless radial displacement at harmonics (l, m) and amplitude of the load height, respectively; both are scaled by planetary radius r_s.

Similarly, surface gravitational load Love number $k_l(t)$ can be derived as

$$k_l(t) = (2l+1)\frac{\phi'_{lm}(t)}{\delta} - 1, \tag{38}$$

where $\phi'_{lm}(t)$ represents the expansion coefficient of dimensionless surface gravitational potential at harmonics (l, m) that includes contributions from both the applied load σ_0 and radial displacements of the mantle (i.e., at the surface and CMB for incompressible mantle).

It is worthwhile to point out that $u_r(t, \theta, \varphi)$ and $\phi(t, \theta, \varphi)$ are calculated at the surface on the CitcomSVE grid in numerical modeling. To compute the Love numbers $h_l(t)$ and $k_l(t)$ using $u'_{rlm}(t)$ and $\phi'_{lm}(t)$ in Equations 37 and 38, the grid-based solutions at different times need to be expanded in spherical harmonic domain using Equation 30. For loading at a single harmonic (l, m) (i.e., Equation 31) on a planet with spherically symmetric mantle structure, the responses in radial displacement $u_r(t, \theta, \varphi)$ and gravitational potential $\phi(t, \theta, \varphi)$ occur at the same forcing harmonic (l, m). In numerical solutions such as those from CitcomSVE, non-zero responses occur at non-forcing harmonics, and they are referred to as dispersion errors of the numerical solutions (e.g., Zhong et al., 2003). It should be pointed out that when lateral variation in either elastic moduli or viscosity is present in the mantle, mode-coupling will lead to responses at non-forcing harmonics in addition to forcing harmonic (e.g., Qin et al., 2014).

Calculations of surface horizontal displacement load Love number $l_l(t)$ in numerical modeling are more complicated. Given the applied potential in Equation 35, dimensionless surface horizontal displacements scaled by planetary radius r_s can be written as

$$u'_\theta(t, \theta, \varphi) = \frac{l_l(t)}{g}\frac{4\pi G\rho_0 r_s \delta}{(2l+1)}\frac{\partial \overline{P}_{lm}(\theta, \varphi)}{\partial \theta}, \quad u'_\varphi(t, \theta, \varphi) = \frac{l_l(t)}{g}\frac{4\pi G\rho_0 r_s \delta}{(2l+1)\sin\theta}\frac{\partial \overline{P}_{lm}(\theta, \varphi)}{\partial \varphi}. \tag{39}$$

Table 2
Comparison of Load Love Numbers h_l, k_l, and l_l Between CitcomSVE and Semi-Analytical Solutions

Case[a]	$h_l(0)$[b]	$k_l(0)$	$\|l_l(0)\|$	$h_l(40)$	$k_l(40)$	$\|l_l(40)\|$
V1_*l*1*m*0	−1.0160 (−1.0158)	−1.0000 (−1.0000)	7.6021e−2 (7.5790e−2)	−1.1885 (1.1882)	−1.0000 (−1.0000)	0.89380 (0.89330)
V1_*l*2*m*0	−0.58407 (−0.58415)	−0.32130 (−0.32144)	0.14519 (0.14519)	−1.9602 (−1.9524)	−0.98723 (−0.98272)	0.86683 (0.86634)
V1_*l*2*m*1	0.10913 (0.10940)	1.0196 (1.0197)	3.9738e−3 (4.0324e−3)	0.38790 (0.39038)	1.3670 (1.3692)	5.2093e−2 (5.1003e−2)
V1_*l*3*m*1	−0.61582 (−0.61573)	−0.23106 (−0.23097)	0.061337 (0.061328)	−2.7502 (−2.7498)	−0.98794 (−0.98786)	0.50350 (0.50341)
V1_*l*4*m*0	−0.60058 (−0.60060)	−0.17103 (−0.17082)	0.036882 (0.036874)	−3.5422 (−3.5418)	−0.98902 (−0.98883)	0.33600 (0.33593)
V1_*l*8*m*0	−0.62946 (−0.62980)	−0.094564 (−0.093227)	0.013617 (0.013603)	−6.6122 (−6.6165)	−0.97722 (−0.97721)	0.14607 (0.14609)
V1_*l*16*m*0	−0.69976 (−0.70201)	−0.059430 (−0.053586)	3.9928e−3 (3.9887e−3)	−11.640 (−11.675)	−0.88891 (−0.88824)	6.6421e−2 (6.6335e−2)
V2_*l*1*m*0	−1.0160 (−1.0158)	−1.0000 (−1.0000)	7.6021e−2 (7.5790e−2)	−1.1656 (−1.1654)	−1.0000 (−1.0000)	0.55725 (0.55700)
V2_*l*2*m*0	−0.58407 (−0.58415)	−0.32130 (−0.32144)	0.14519 (0.14519)	−1.8643 (−1.8666)	−0.94348 (−0.94490)	0.59453 (0.59579)
V2_*l*2*m*1	0.10913 (0.10940)	1.0196 (1.0197)	3.9738e−3 (4.0324e−3)	0.32095 (0.32229)	1.2952 (1.2963)	4.9591e−2 (5.0316e−2)
V2_*l*3*m*1	−0.61582 (−0.61573)	−0.23106 (−0.23097)	6.1337e−2 (6.1328e−2)	−2.6524 (−2.6524)	−0.95402 (−0.95406)	0.35805 (0.35810)
V2_*l*4*m*0	−0.60058 (−0.60060)	−0.17103 (−0.17082)	3.6882e−2 (3.6874e−2)	−3.4335 (−3.4333)	−0.95898 (−0.95886)	0.25148 (0.25157)
V2_*l*8*m*0	−0.62946 (−0.62980)	−0.094564 (−0.093228)	1.3617e−2 (1.3603e−2)	−6.4253 (−6.4305)	−0.94966 (−0.94973)	8.7371e−2 (9.7414e−2)
V2_*l*16*m*0	−0.69976 (−0.70201)	−0.059430 (−0.053586)	3.9928e−3 (3.9887e−3)	−10.953 (−11.001)	−0.83686 (−0.83699)	2.2064e−2 (2.1998e−2)

[a]Case number follows the following notation: V1 for constant mantle viscosity of 10^{21} Pas, and V2 for including 100 km thick lithosphere of 10^{26} Pas; *l*3*m*1 stands for loading harmonic at $l = 3$ and $m = 1$. [b]Load Love numbers are given at times 0 and 40 Maxwell time. Each entry has semi-analytical and CitcomSVE solutions in and out of the parentheses, respectively. For CitcomSVE solutions, only results from resolution R6 (i.e., 12 × 64 × 128 × 128) are given here, and for results of other resolutions, see Table S1. Also see Figures 2–4.

Considering the integral relationship (e.g., Dahlen & Tromp, 1998),

$$\frac{1}{l(l+1)}\oint\left\{\left[\frac{\partial\overline{P}_{lm}(\theta,\varphi)}{\partial\theta}\right]^2+\left[\frac{1}{\sin\theta}\frac{\partial\overline{P}_{lm}(\theta,\varphi)}{\partial\varphi}\right]^2\right\}\sin\theta\mathrm{d}\theta\mathrm{d}\varphi=1, \tag{40}$$

where the integration is for the whole spherical surface, we may determine $l_l^2(t)$ as

$$l_l^2(t)=\left[\frac{(2l+1)g}{4\pi G\rho_0 r_s\delta}\right]^2\frac{1}{l(l+1)}\oint\left\{\left[u'_\theta(t,\theta,\varphi)\right]^2+\left[u'_\varphi(t,\theta,\varphi)\right]^2\sin\theta\mathrm{d}\theta\mathrm{d}\varphi\right\}. \tag{41}$$

Note that this only computes the square of Love number $l_l(t)$ from numerical models. Similar techniques were used in evaluating characteristic horizontal flow velocity in Stokes' flow calculations (Zhong et al., 2008).

3.1.3. Benchmark Results

We have computed a total of 84 different model cases using CitcomSVE for six different sets of numerical resolutions, seven different loading harmonics, and two different viscosity structure (Table 2). Six different numerical resolutions of R1-R6 are for 12 × (32 × 32 × 32), 12 × (48 × 48 × 48), 12 × (64 × 64 × 64), 12 × (96 × 96 × 96), 12 × (64 × 96 × 96) and 12 × (64 × 128 × 128), respectively, where the first number, 12, indicates the number of spherical caps that the spherical surface is divided into, and the subsequent numbers indicate the number of elements in each cap in the radial and two horizontal directions (Figures 1a and 1b) (Zhong et al., 2000, 2008). Seven different loading harmonics are for (1, 0), (2, 0), (2, 1), (3, 1), (4, 0), (8, 0), and (16, 0) where the first and second numbers in a parenthesis (l, m) indicate spherical harmonic degree l and order m, respectively. Viscosity model V1 is for uniform mantle viscosity and V2 is for a 100 km thick high viscosity lithosphere (10^{26} Pas) overlying a uniform mantle viscosity of 10^{21} Pas, respectively. Each case can be named by its viscosity structure, loading harmonic and numerical resolution, for example, case V1_l2m0_R1 corresponds to a case where viscosity V1, loading harmonic at (2, 0) and resolution R1 are used.

For each case, CitcomSVE is used to compute time-dependent solutions of 3-D displacement field of the mantle and gravitational potential at the surface, in response to a single harmonic surface loading (i.e., Equation 31).

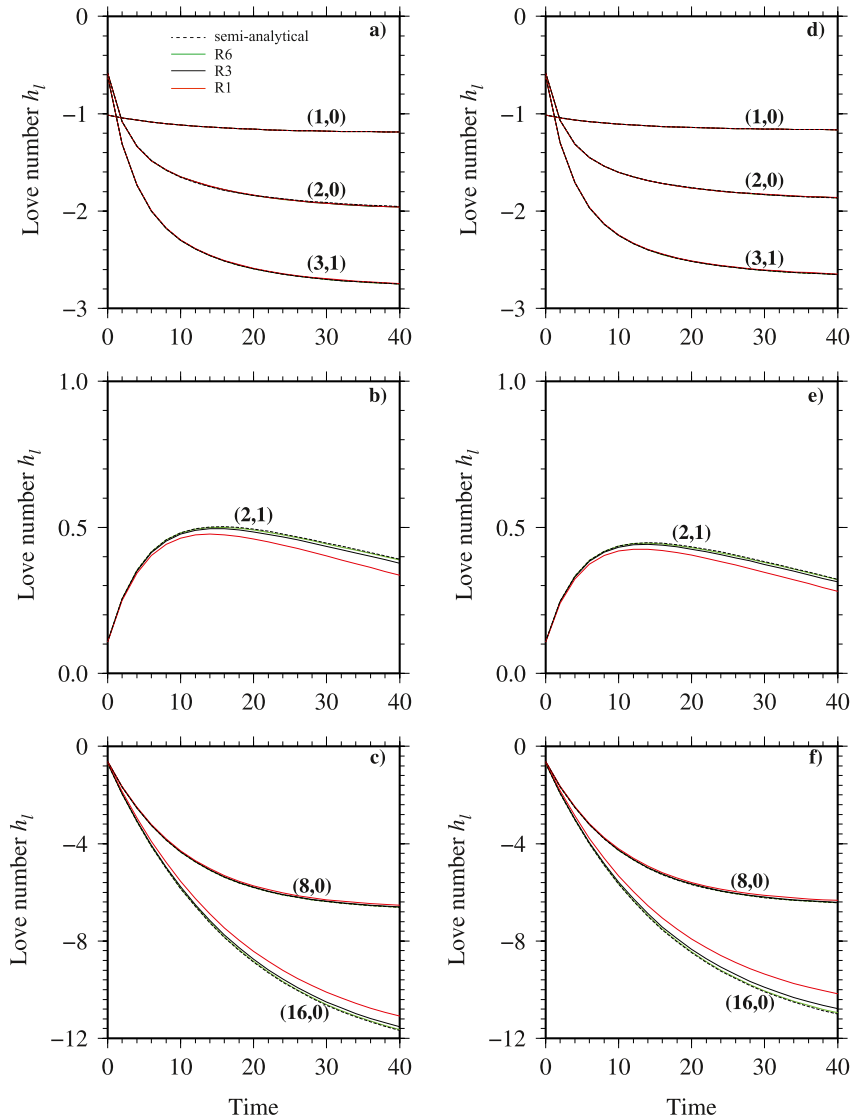

Figure 2. Radial displacement load Love numbers h_l as a function of time from semi-analytical solutions and CitcomSVE solutions with resolutions R1, R3, and R6 for loading harmonics $(l, m) = (1, 0)$, $(2, 0)$, and $(3, 1)$ (a), $(2, 1)$ (b), and $(8, 0)$ and $(16, 0)$ (c) for viscosity model V1 (i.e., constant mantle viscosity). Panels (d–f) are the same as (a–c) but for viscosity model V2 (i.e., with a 100 km thick lithosphere). R1, R3, and R6 are for grids $12 \times (32 \times 32 \times 32)$, $12 \times (64 \times 64 \times 64)$, and $12 \times (64 \times 128 \times 128)$, respectively. Note that the semi-analytical solutions and numerical solutions from R1, R3, and R6 for calculations with (1,0), (2,0), and (3,1) are nearly identical in (a, d).

Each case is computed for 40 Maxwell times (i.e., 40α or non-dimensional time of 40), using non-dimensional time increment of 0.2. Time-dependent Love numbers $h_l(t)$, $k_l(t)$, and $l_l^2(t)$ are computed, using Equations 37, 38 and 41, respectively. Figures 2–4 show $h_l(t)$, $k_l(t)$, and $l_l^2(t)$, respectively, for cases with different loading harmonics and different numerical resolutions, together with semi-analytical solutions (A et al., 2013; Han & Wahr, 1995). Table 2 shows both numerical and analytical results of these Love numbers at $t = 0$ and 40 for a selected set of cases (Table S1 for all the cases). Note that solutions at $t = 0$ represent the elastic responses of the mantle, and the responses generally increase with time due to viscous relaxation (Figures 2–4).

The numerical solutions generally agree well with semi-analytical solutions for nearly all the cases. For long-wavelength loading (e.g., l1m0, l2m0, l3m1, and l4m0), numerical solutions with three different resolutions R1, R3, and R6 nearly overlap with semi-analytical solutions (Figures 2–4). Note that l1m0 loading requires calculations of degree-1 motion in the center of mass reference frame (see Section 2.4.1). However, for relatively short wavelengths (e.g., l8m0 and l16m0), numerical results for resolution R1 show clear deviation from semi-analytical

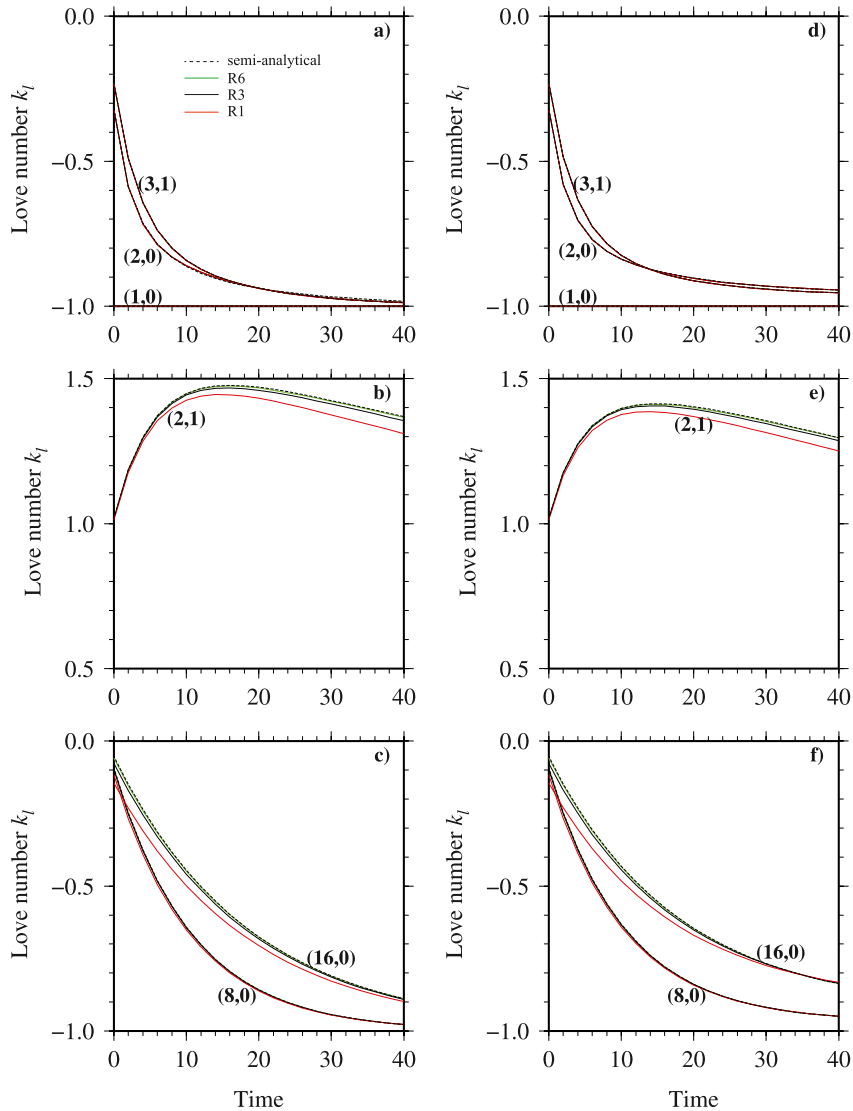

Figure 3. The same as Figure 2 except for gravitational load Love numbers k_l.

solutions, but the agreement improves significantly as numerical resolution increases (Figures 2–4). In particular, for l2m1 cases with polar wander, calculations with resolutions R1 and R3 have significant numerical errors, but calculation with R6 resolution still delivers remarkable fit to the semi-analytical solution, suggesting that polar wander is more challenging to compute in numerical models (e.g., Paulson et al., 2005; A et al., 2013). In all these calculations, while the high viscosity lithosphere in V2 cases reduces the response relative to the uniform viscosity V1 cases, it does not appear to deteriorate the accuracy of numerical solutions. Note that the load Love number for horizontal displacement is presented as $|l_l(t)|$, because CitcomSVE only determines $l_l^2(t)$ (see Equation 41).

We have formally determined numerical errors by computing amplitude and dispersion errors (e.g., A et al., 2013; Zhong et al., 2003). Amplitude error ε_a and dispersion error ε_d are computed using the following equations:

$$\varepsilon_a = \frac{\int_0^T |S_n(l_0, m_0, t) - S_{sa}(l_0, m_0, t)|\,\mathrm{d}t}{\int_0^T |S_{sa}(l_0, m_0, t)|\,\mathrm{d}t}, \tag{42}$$

$$\varepsilon_d = \frac{\int_0^T \max\left[|S_{n(l,m,t)}|\right]\mathrm{d}t}{\int_0^T |S_{sa}(l_0, m_0, t)|\,\mathrm{d}t}, \tag{43}$$

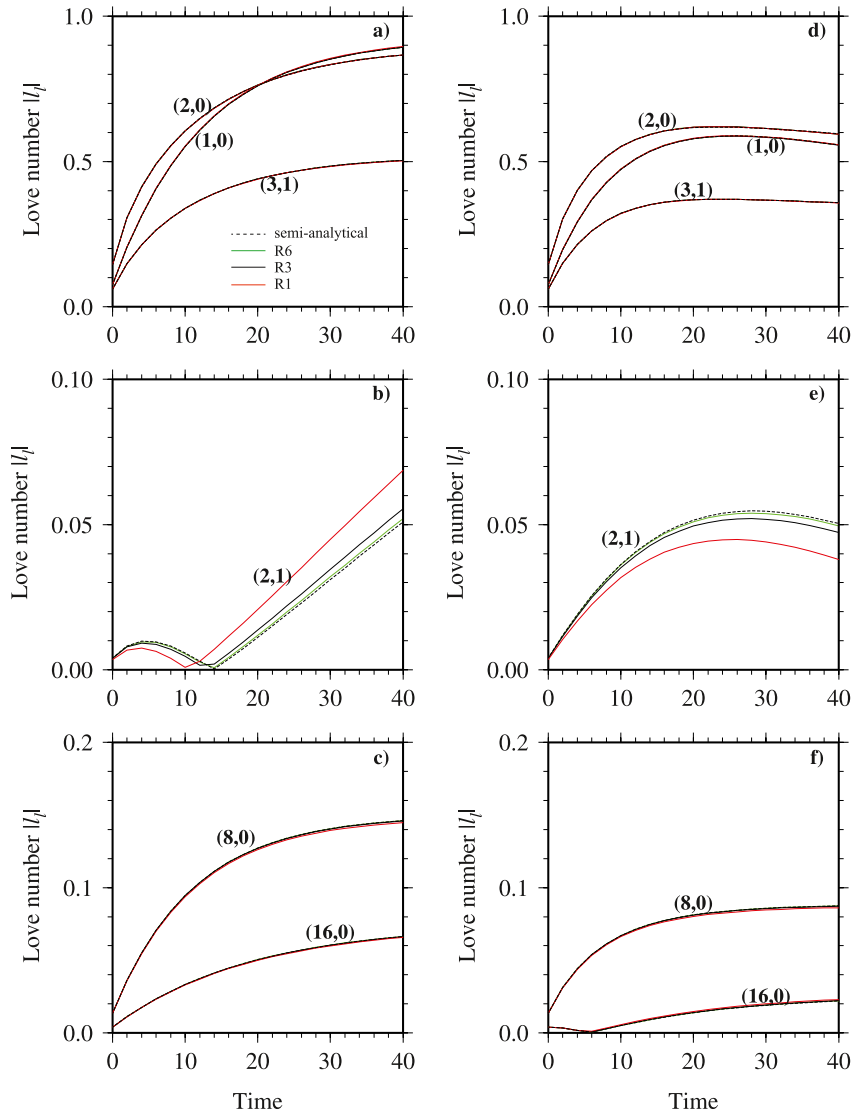

Figure 4. The same as Figure 2 except for horizontal load Love numbers $|l_l|$.

where l_0 and m_0 represent the loading harmonic degree and order, S_n and S_{sa} are solutions of load Love numbers from CitcomSVE and semi-analytical methods, respectively, T is the total model time (i.e., 40), and in Equation 43 for the dispersion error, max represents finding the maximum value for all the non-loading harmonic degree l and order m. For the spherically symmetric mantle structure that is considered here, the response should only occur at the loading harmonic. Therefore, amplitude error ε_a measures the accuracy at the loading harmonic, where dispersion error ε_d measures the accuracy at other harmonics. Note that the errors as defined in Equations 42 and 43 are similar to norm-1 errors.

The errors are computed for each case with different resolutions and are listed in Table S1. The amplitude errors of three load Love numbers are presented in Figure 5 as a function of numerical resolution (i.e., the horizontal grid size ranging from ~200 to ~50 km at the surface for resolutions R1–R6) for all calculations with different loading harmonics and viscosity structures V1 and V2. For most of the cases at different loading harmonics, the amplitude errors decrease with decreasing horizontal grid size with a slope of ~2 in the log-log plot of Figure 5, suggesting that the errors scale with the square of grid size, indicating a second order of accuracy as expected for trilinear elements in CitcomS (e.g., Zhong et al., 2008). However, as exceptions, l2m0 calculations do not show any significant dependence on grid size, and similar behaviors can also be seen for $h_l(t)$ for l1m0 calculations and for other long-wavelength loading cases with small grid size (Figure 5). We think that this behavior for errors

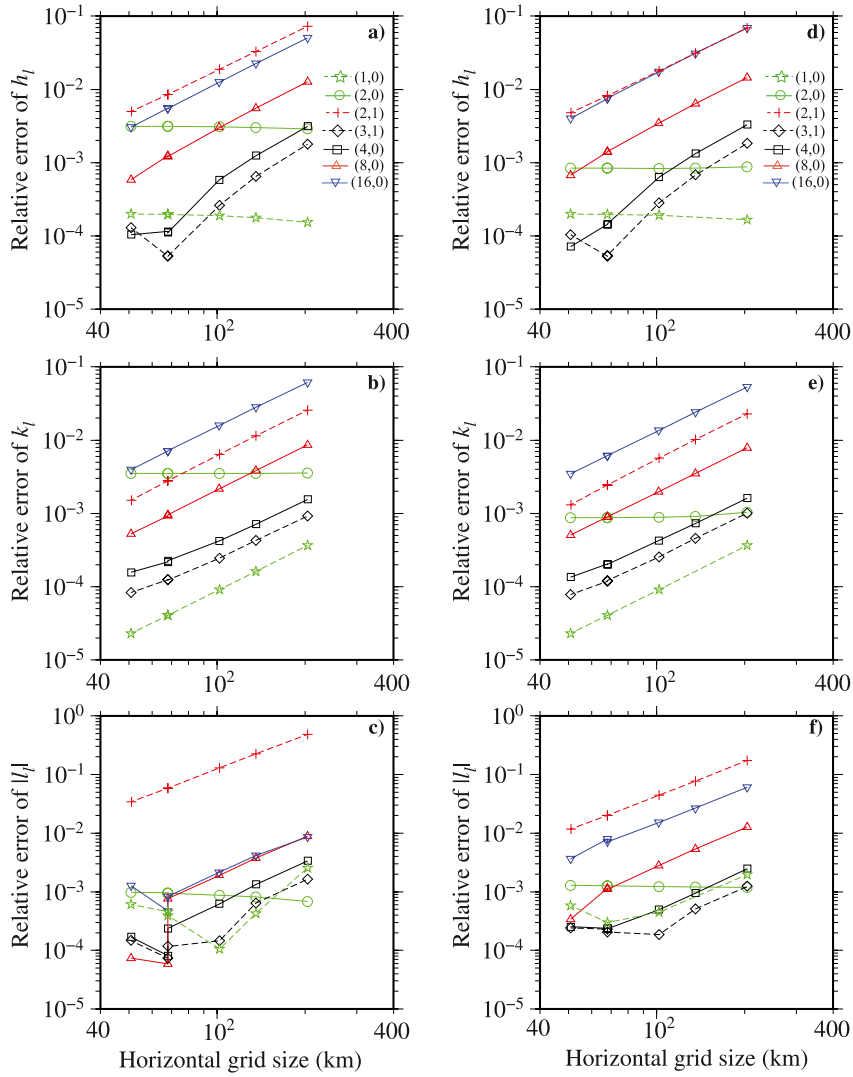

Figure 5. Relative errors of load Love numbers h_l (a), k_l (b), and $|l_l|$ (c) as a function of numerical resolutions (i.e., for R1–R6 or horizontal grid resolution of approximately 200–50 km) for 7 different loading harmonics for viscosity model V1. Panels (d–f) are the same as (a–c) but for viscosity model V2. Note that resolutions R4 and R5 have the same horizontal resolution but different radial resolution.

arises because the error-limiting factor at these long wavelengths is not grid size but convergence tolerance of the iterative solution of the equations of the motion, which is set to 10^{-3} for all the calculations here. These calculations show that <1% of amplitude errors are readily achieved with modest resolution of ~60 km grid size except for horizontal displacement Love number $l_l(t)$ for l2m1 (i.e., polar wonder) (Figures 5c and 5f). It should be noted that the dispersion errors are generally significantly smaller than amplitude errors (Table S1).

For case V1_l2m0_R1, we performed two additional calculations with different non-dimensional time increment Δt of 0.1 and 0.4, and we found that the errors are insensitive to Δt ranging from 0.1 to 0.4 (Table S1). We think that the error insensitivity to Δt for case V1_l2m0_R1 arises because the error-limiting factor for this case may be the convergence tolerance level and not time resolution Δt, similar to how the errors for long-wavelength loading are insensitive to spatial resolution (Figure 5). We also performed calculations that demonstrate that the net rotation removal (see Section 2.4.2) is essential for producing accurate horizontal displacement, although it has no effect on radial displacement and gravitational potential calculations.

3.2. Tidal Loading at Degree Two

3.2.1. Definition of the Tidal Loading Problem

In the second example problem, a degree-2 potential V_a (e.g., a tidal potential, see Equation 2) is applied to the mantle (see Equation 4) as a step-function in time, in a dimensionless form:

$$V_a(t, r, \theta, \varphi) = V_0 r^2 p_{20}(\theta) H(t), \tag{44}$$

where $V_o = 10^{-6}$ is the dimensionless amplitude of the applied potential (see Section 2.4.6 for the normalization), $p_{20}(\theta)$ is the modified Legendre polynomial as defined in Equation 29, and $H(t)$ is the Heaviside function. For simplicity, only the degree-2 and order-0 tidal potential is considered, because of its dominance over other higher order tidal potentials (e.g., Wahr et al., 2009). Although the potential is applied at all the radius r, for incompressible medium as in our example here, the potential only needs to be applied at the surface and CMB where there is a density change. It should be noted that CitcomSVE has been used to compute tidal response for the Moon with 3-D mantle structure (Zhong et al., 2012), and in particular, the tidal response solutions for 3-D mantle structure from CitcomSVE are in excellent agreement with those from a perturbation solution method (Qin et al., 2014, 2016).

The benchmark results are presented in terms of tidal Love numbers $h'_2(t)$, $k'_2(t)$, and $l'_2(t)$ at degree 2 for radial displacement, gravitational potential, and horizontal displacement, respectively. The tidal Love numbers are defined similarly to those for load Love numbers in Equations 37, 38 and 41 except for $(2l + 1)$ factor.

$$h'_2(t) = \frac{g}{4\pi G \rho_0 r_s} \frac{u'_{r20}(t)}{V_0} \tag{45}$$

$$k'_2(t) = \frac{\phi'_{20}(t)}{V_0} - 1, \tag{46}$$

$$l'^2_2(t) = \left[\frac{g}{4\pi G \rho_0 r_s V_0}\right]^2 \frac{1}{6} \oint \left\{ \left[u'_\theta(t, \theta, \varphi)\right]^2 + \left[u'_\varphi(t, \theta, \varphi)\right]^2 \right\} \sin\theta \mathrm{d}\theta \mathrm{d}\varphi, \tag{47}$$

where all the variables were defined following Equations 37, 38 and 41. For example, $u'_{r20}(t)$ and $\phi'_{20}(t)$ are the expansion coefficients of dimensionless surface radial displacement and gravitational potential for harmonics (2, 0), respectively. $\phi'_{20}(t)$ includes contributions from both the applied potential and radial displacements of the mantle (i.e., at the surface and CMB for incompressible mantle). Note that all these dimensionless quantities are directly output from CitcomSVE. Model parameters used for these tidal Love number calculations are the same as those for the first example problem of surface loading (Table 1).

3.2.2. Benchmark Results

We have computed a total of 8 different model cases using CitcomSVE for 4 different sets of numerical resolutions (i.e., R2, R3, R5, and R6; see Section 3.1.3) and two different viscosity structures V1 and V2 (Table 3). For each case, CitcomSVE is used to compute the time-dependent solutions of the 3-D displacement field of the mantle and the gravitational potential at the surface for 400 Maxwell times using dimensionless time increment Δt of 0.5. Time-dependent Love numbers $h'_2(t)$, $k'_2(t)$, and $l'^2_2(t)$ are then computed, using Equations 45–47, respectively. Figures 6a–6c show $h'_2(t)$, $k'_2(t)$, and $|l'_2(t)|$, respectively, for V1 cases (i.e., homogeneous mantle viscosity) with different numerical resolutions R3 and R6, together with semi-analytical solutions (Qin et al., 2014). Table 3 shows both numerical and semi-analytical results of these Love numbers at $t = 0$ and 400. Degree-2 tidal Love numbers from CitcomSVE are nearly identical (i.e., overlapping) to the semi-analytical solutions (Figures 6a–6c), similar to that in the (2,0) load Love number calculations. Elastic tidal responses or Love numbers (i.e., at $t = 0$) are generally small, but the responses increase with time to steady state values after ~50 Maxwell times. Model results for V2 cases (i.e., with 100 km thick high viscosity lithosphere) are similar to those for V1 cases, but the amplitudes of the response are reduced slightly (see Table 3).

Since either elastic tidal response (i.e., at $t = 0$) or its fluid limit (i.e., fluid Love numbers), is mostly interested in tidal response modeling, we only calculate relative numerical errors for elastic tidal Love numbers (i.e., at $t = 0$) and for fluid Love numbers (i.e., at $t = 400$) for both V1 and V2 cases. Relative errors for all three degree-2

Table 3
Comparison of Degree-2 Tidal Love Numbers h'_2, k'_2 and l'_2 Between CitcomSVE and Semi-Analytical Solutions

Case[a]	$h'_2(0)$[b]	$k'_2(0)$	$\|l'_2(0)\|$	$h'_2(400)$	$k'_2(400)$	$\|l'_2(400)\|$
V1_SA	0.72664	0.40541	0.15634	2.1078	1.1078	0.73864
V1_R6	0.72652 (1.6e−4, 3.5e−5)	0.40526 (3.8e−4, 7.2e−5)	0.15633 (5.4e−5, –)	2.1075 (1.3e−4, 1.2e−4)	1.1075 (2.4e−4, 1.2e−4)	0.73853 (1.4e−4, –)
V1_R5	0.72651 (1.7e−4, 6.1e−5)	0.40519 (5.5e−4, 1.3e−4)	0.15632 (5.1e−4, –)	2.1073 (2.3e−4, 2.1e−4)	1.1073 (4.3e−4, 2.1e−4)	0.73844 (2.7e−4, –)
V1_R3	0.72623 (5.6e−4, 1.4e−4)	0.40484 (1.4e−3, 2.9e−4)	0.15626 (5.1e−4, –)	2.1067 (5.1e−4, 4.7e−4)	1.1067 (9.8e−4, 4.7e−4)	0.73821 (5.8e−4, –)
V1_R2	0.72590 (1.0e−3, 2.4e−4)	0.40439 (2.5e−3, 5.1e−4)	0.15621 (8.3e−4, –)	2.1059 (9.1e−4, 8.4e−4)	1.1059 (1.7e−3, 8.4e−4)	0.73789 (1.0e−3, –)
V2_SA	0.72664	0.40541	0.15634	2.0359	1.0708	0.54673
V2_R6	0.72652 (1.6e−4, 3.5e−5)	0.40526 (3.8e−4, 7.2e−5)	0.15633 (5.4e−5, –)	2.0359 (1.8e−5, 1.2e−4)	1.0707 (1.0e−4, 1.2e−4)	0.54677 (7.0e−5, –)
V2_R5	0.72651 (1.7e−4, 6.1e−5)	0.40519 (5.5e−4, 1.3e−4)	0.15632 (5.1e−4, –)	2.0357 (8.1e−5, 2.1e−4)	1.0705 (2.9e−4, 2.1e−4)	0.54671 (3.3e−5, –)
V2_R3	0.72623 (5.6e−4, 1.4e−4)	0.40484 (1.4e−3, 2.9e−4)	0.15626 (5.1e−4, –)	2.0351 (3.6e−4, 4.6e−4)	1.0699 (8.4e−4, 4.6e−4)	0.54658 (2.8e−4, –)
V2_R2	0.72590 (1.0e−3, 2.4e−4)	0.40439 (2.5e−3, 5.1e−4)	0.15621 (8.3e−4, –)	2.0343 (7.6e−4, 8.2e−4)	1.0691 (1.6e−3, 8.2e−4)	0.54642 (5.6e−4, –)

[a]Case number follows the following notation: V1 for constant mantle viscosity of 10^{21} Pas, and V2 for including 100 km thick lithosphere of 10^{26} Pas; SA stands for semi-analytical solutions; R2, R3, R5 and R6 are for grids $12 \times 48 \times 48 \times 48$, $12 \times 64 \times 64 \times 64$, $12 \times 64 \times 96 \times 96$, and $12 \times 64 \times 128 \times 128$, respectively. [b]Tidal Love numbers are given at time 0 for the elastic Love number and at time 400 Maxwell time for the fluid Love number. For each numerical calculation, the number outside of the parentheses is the Love number, while the two numbers inside the parentheses are for amplitude and dispersion errors, respectively. Note that the elastic solutions (i.e., at $t = 0$) are independent of viscosity structure, so V1 and V2 calculations produce the same elastic solutions for a given resolution. Also, dispersion errors cannot be computed for l Love numbers. Also see Figure 6.

elastic and fluid tidal Love numbers are generally smaller than 3×10^{-3}, even for relatively coarse resolution R2 (~140 km horizontal grid size) (Table 3), and the errors decrease with increasing resolution with a slope of ~2 in the log-log plots of errors versus grid size (Figures 6d–6f), indicating that CitcomSVE performs well for tidal response calculations. Note that the elastic Love numbers for viscosity structure V1 are the same as those for viscosity structure V2, because elastic Love numbers do not depend on viscosity structure.

3.3. Glacial Isostatic Adjustment Using ICE-6G and VM5a

3.3.1. Definition of the GIA Problem

The third example problem uses the deglaciation history model ICE-6G for the last 26 ky (i.e., thousand years) as the surface loads, together with viscosity model VM5a (Peltier et al., 2015), and considers the effects of polar wander, apparent center of mass motion and sea-level equation (see Section 2.4). The current version of CitcomSVE was used for this benchmark problem in Kang et al. (2022), and here we will present additional calculations with different temporal and spatial resolutions, and also compute radial displacement rate and horizontal displacements and rates. The model parameters except for VM5a viscosity are the same as in previous two example problems (Table 1).

A glaciation period of 96 ky is added before the ICE-6G deglaciation history, so that the GIA model calculation is for a total of 122 ky time duration. The glaciation history has two stages. In the first stage from 122 kybp (kybp stands for thousand years before the present) to 104 kybp, the ice increases linearly with time from zero everywhere to that of the present-day ice distribution. In the second stage from 104 kybp to 26 kybp, the ice continues to grow linearly with time to the last glacial maximum (i.e., LGM) with the ice that grows primarily in North America and Fennoscandia. Mantle viscosity model VM5a has five viscosity layers from the surface to CMB: a 60 km thick elastic lithosphere with very high viscosity (10^{26} Pas), and 10^{22}, 4.853×10^{20}, 1.5048×10^{21}, and 3.095×10^{21} Pas for depth ranges of 60–100 km, 100–670 km, 670–1,170 km, and 1,170 km-CMB, respectively (Table 1) (Peltier et al., 2015).

Five GIA cases (i.e., GIA_R1, GIA_R2, GIA_R3, GIA_R2_LT and GIA_R2_HT, see Table 4) are computed using CitcomSVE with three different spatial (i.e., $12 \times 48 \times 48 \times 48$, $12 \times 48 \times 80 \times 80$, and $12 \times 64 \times 128 \times 128$ for cases GIA_R1, GIA_R2, and GIA_R3, respectively) and three different temporal resolutions (i.e., Δt of 50, 100, and 250 years for GIA_R2_HT, GIA_R2, and GIA_R2_LT, respectively). Note that HT and LT stand for high and low resolution in time, respectively. Also note that the $12 \times 48 \times 80 \times 80$ grid (i.e., GIA_R2) as in Kang et al. (2022) leads to horizontal resolution of ~81 km at the surface and ~45 km at the CMB, and radial

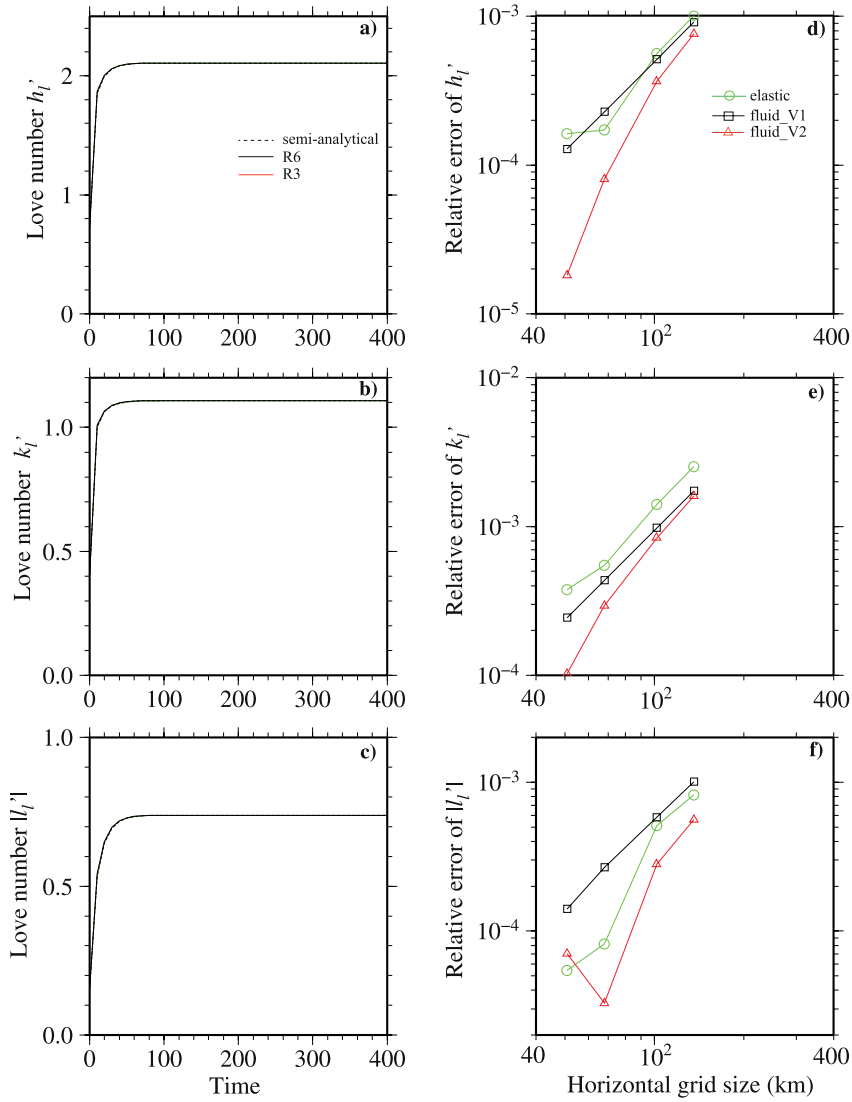

Figure 6. (2,0) tidal Love numbers h_l' (a), k_l' (b) and $|l_l'|$ (c) as a function of time from semi-analytical solutions and CitcomSVE solutions with resolutions R3 and R6 for viscosity model V1 (i.e., constant mantle viscosity). Relative errors of tidal Love numbers h_l' (d), k_l' (e), and $|l_l'|$ (f) as a function of numerical resolutions (i.e., for R2, R3, R5, and R6) at $t = 0$ (i.e., elastic tidal Love numbers) and $t = 400$ (i.e., fluid tidal Love numbers) for viscosity models V1 and V2. Note that the elastic Love numbers are the same for models V1 and V2 and that the semi-analytical solutions and numerical solutions from R3 and R6 for the Love numbers are overlapped in (a–c).

resolution of ~60 km, but grid refinement is employed such that the radial resolution is 20 km for the 100 km thick lithosphere and is ~40 km for the upper mantle. Case GIA_R3 has ~51 km (or ~0.5°) and ~28 km horizontal resolution at the surface and CMB, respectively.

As discussed in Section 2.3, the gravitational potential is computed in the spherical harmonic domain in CitcomSVE calculations and is then projected back to the grid in solving for displacement field. This process can be computationally expensive. In our calculations here, the gravitational potential is only computed for up to degrees and orders 32 for all three spatial resolutions. On the other hand, semi-analytical solutions are obtained using spherical harmonic degrees and orders up to 100.

3.3.2. Benchmark Results

We compute the 3-component surface cumulative displacement and displacement rate at three different times (i.e., the present-day, 15, and 26 kybp) from CitcomSVE and the semi-analytical method and determine the difference

Table 4
Relative RMS Errors for GIA Surface 3-Component Displacement and Rate

	GIA_R1	GIA_R2	GIA_R3	GIA_R2_HT	GIA_R2_LT
Δt (years)	100	100	100	50	250
Grid resolution[a]	R1	R2	R3	R2	R2
Time steps	1,220	1,220	1,220	2,440	488
CPU time (hour)[b]	0.345	1.23	4.58	2.13	0.643
$\varepsilon_{d\_r}(0)$ (%)[c]	4.13	2.05	1.24	2.05	2.05
$\varepsilon_{d\_h}(0)$ (%)	10.8	1.49	0.70	5.82	0.88
$\varepsilon_{r\_r}(0)$ (%)	11.1	5.88	4.06	5.84	6.36
$\varepsilon_{r\_h}(0)$ (%)	27.9	6.65	5.73	17.6	6.60
ε_{d_r}(15 kybp) (%)	3.94	2.00	1.26	2.00	2.01
ε_{d_h}(15 kybp) (%)	7.40	1.30	0.70	3.89	1.01
ε_{r_r}(15 kybp) (%)	6.95	4.69	4.09	4.03	7.59
ε_{r_h}(15 kybp) (%)	2.32	1.79	1.46	1.57	3.16
ε_{d_r}(26 kybp) (%)	3.80	1.93	1.23	1.93	1.93
ε_{d_h}(26 kybp) (%)	5.02	1.00	0.58	2.61	0.84
ε_{r_r}(26 kybp) (%)	4.31	2.21	1.37	2.20	2.20
ε_{r_h}(26 kybp) (%)	5.39	1.20	0.90	3.15	1.03

[a]Grid resolution R1, R2, and R3 correspond to grids $12 \times 48 \times 48 \times 48$, $12 \times 48 \times 80 \times 80$, and $12 \times 64 \times 128 \times 128$, respectively. [b]All the cases are computed using 96 cores on NCAR supercomputer Cheyenne. CPU time reported here includes all the calculation time for each case. [c]Errors ε_{d_r} and ε_{d_h} are the RMS percentage errors for surface cumulative displacement in radial and horizontal directions, respectively. Errors ε_{r_r} and ε_{r_h} are the RMS percentage errors for surface displacement rate in radial and horizontal directions, respectively. The errors are given at present-day (time 0), 15 kybp, and 26 kybp.

between these two solution methods. Figures 7 and 8 show the present-day's north-south, east-west, and radial components of the cumulative displacement and displacement rate, respectively, from CitcomSVE for Case GIA_R2. Since the model is assumed to have zero topography and zero ice at 122 kybp (i.e., at the beginning of the model), the cumulative radial displacement (Figure 7c) at the present-day is predominated by large negative (i.e., depression) values in Greenland and East Antarctica, as expected. However, in reality, Greenland and Antarctica may have maintained significant ice sheets for a long geological time, and the ice-induced depression in Greenland and Antarctica may have occurred long before the last glacial cycle. About 100 m depression is also seen at the center of the former North American ice sheet, suggesting that the region still has significant surface topography to be recovered. Cumulative displacements in horizontal directions mainly occur in the polar regions but with much smaller amplitude than the radial displacement (Figures 7a and 7b). Large positive radial displacement rates (i.e., uplift) at the present-day occur in North America, Fennoscandia and West Antarctica (Figure 8c), suggesting active uplift following more recent deglaciation in these regions. The horizontal displacement rates are much smaller than the radial, and they are most significant in North America (Figures 8a and 8b). The directions of the horizontal displacements are consistent with the uplift motion at the center of North American ice sheet.

The differences (i.e., errors) in cumulative displacements and displacement rates between CitcomSVE and semi-analytical solutions are much smaller than the solutions themselves and the errors occur mostly where the responses are large (Figures 7d–7f, and 8d–8f). The relative RMS difference or error in the spatial domain between CitcomSVE and semi-analytical solutions is defined as:

$$\varepsilon(t) = \sqrt{\frac{\sum [f_{FE}(\theta,\varphi,t) - f_S(\theta,\varphi,t)]^2}{\sum [f_S(\theta,\varphi,t)]^2}}, \tag{48}$$

where $f_{FE}(\theta,\varphi,t)$ and $f_S(\theta,\varphi,t)$ denote the field of interest at a given time t from CitcomSVE and semi-analytical solutions, respectively, and the summation is for all the finite element grid points. Note that the analytical solutions are computed at each of the finite element grid points. Since the horizontal size of each CitcomSVE element is similar from the polar to equatorial regions, each node carries similar weight, justifying a simple summation for all the nodes for computing the errors. Errors for radial component and horizontal components are computed for three different times: the present-day, 15 and 26 kybp. For computing the horizontal error, we square the difference for each horizontal component before adding them for each node.

Table 4 lists the errors for cumulative displacements and displacement rates at these three times for radial and horizontal components for the five GIA cases, together with total CPU time for each case that was computed using 96 cores on NCAR supercomputer Cheyenne. For the present-day surface cumulative displacements and displacement rates of Case GIA_R2 shown in Figures 7 and 8, the displacement errors are ~2% for both horizontal and radial components, while the corresponding errors for the rates are ~6% (Table 4). As will be clarified later, the errors are largely from relatively short wavelengths with spherical harmonic degrees larger than 15. For this case, the errors for 15 and 26 kybp are comparable with those at the present-day. The errors are smaller for cases with higher spatial resolution (e.g., GIA_R1 and GIA_R3 in Table 4), as expected. In general, the errors for the cumulative displacements and rates are slightly larger for the present-day than for 15 and 26 kybp. For spatial resolutions comparable with GIA_R2 or higher, the errors for cumulative displacements are at ~2% or less for both radial and horizontal components, but the errors for the rates are at ~5% or less. However, the errors can exceed 10% for a lower spatial resolution (e.g., GIA_R1) for the horizontal components and rates at the present-day (Table 4). The errors for both cumulative displacements and rates appear to be insensitive to time resolutions, which is surprising. In fact, under most circumstances, Case GIA_R2_HT with $\Delta t = 50$ years

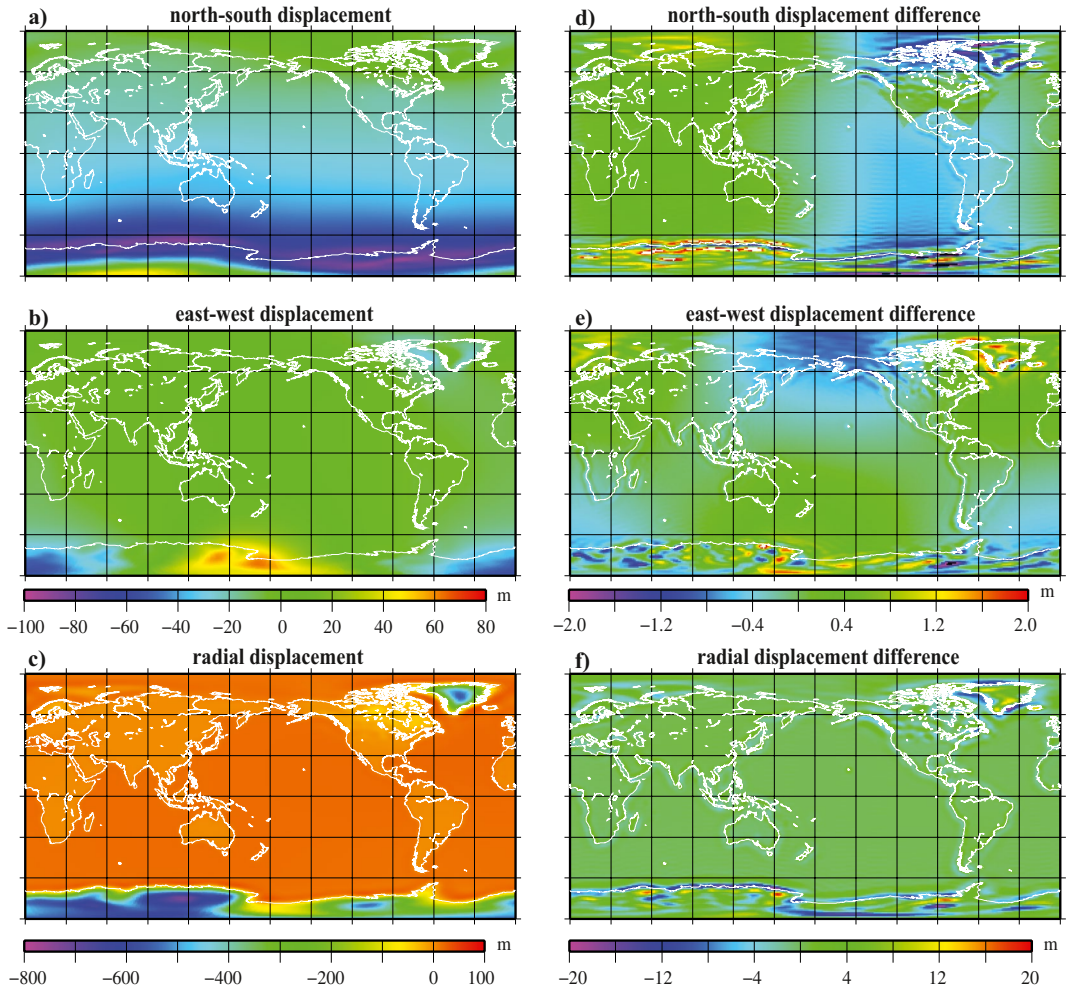

Figure 7. Cumulative surface displacements at the present-day for Case GIA-R2 in north-south (a), east-west (b), and radial (c) directions, and the corresponding difference between Case GIA_R2 and semi-analytical solutions in north-south (d), east-west (e), and radial (f) directions. Note that the south, east and up directions are positive.

produces larger errors, especially for horizontal motions, than Cases GIA_R2_LT with Δt = 250 years and GIA_R2 with Δt = 100 years (Table 4). It appears that Δt from 100 to 250 years is most efficient in computational accuracy and speed.

We also compute and compare cumulative surface radial displacements of different spherical harmonic degrees from CitcomSVE and the semi-analytical solutions, following our previous work (A et al., 2013; Kang et al., 2022; Paulson et al., 2005). The surface displacement field from CitcomSVE is expanded into a set of spherical harmonic coefficients (see Equations 29 and 30 for the spherical harmonic expansion used in CitcomSVE). The degree amplitude for each l is calculated by

$$a_l(t) = \sqrt{\frac{1}{l+1}\sum_{m=0}^{l}\left[C_{lm}(t)^2 + S_{lm}(t)^2\right]}, \tag{49}$$

where C_{lm} and S_{lm} denote the cosine and sine coefficients for the radial displacements at time t. Figures 9a and 9b show the time variations in degree amplitude of surface radial displacement at selected spherical harmonics degrees (l = 1, 2, 5, 9, 16 and 23) for the five CitcomSVE cases and also the semi-analytical solutions. For relatively long wavelengths (l = 1, 2, 5, and 9), the five CitcomSVE cases are nearly identical to each other and to the semi-analytical solution (Figure 9a), but for shorter wavelengths (l = 16 and 23), the results from CitcomSVE cases differ noticeably from each other and from the semi-analytical solutions, especially for relatively low spatial

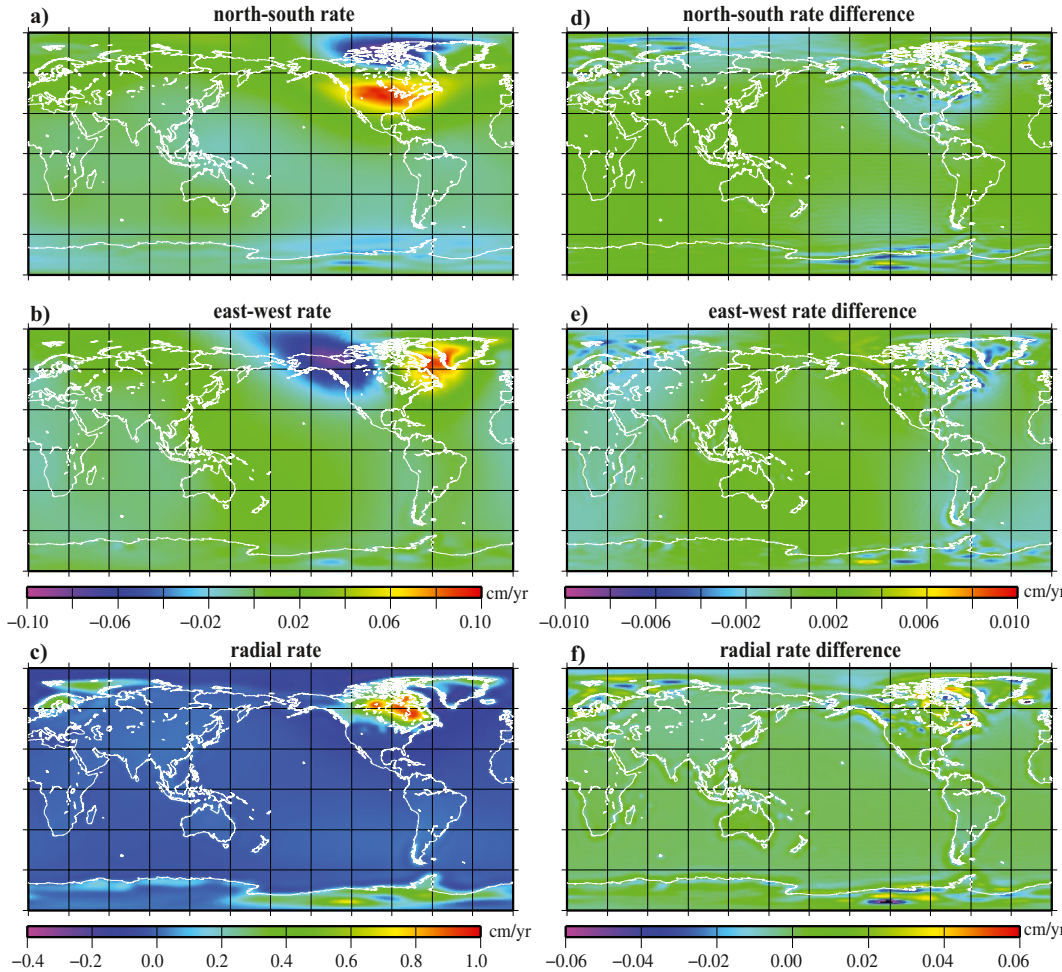

Figure 8. Surface displacement rates at the present-day for Case GIA-R2 in north-south (a), east-west (b), and radial (c) directions, and the corresponding difference between Case GIA_R2 and semi-analytical solutions in north-south (d), east-west (e), and radial (f) directions. Note that the south, east and up directions are positive.

resolution cases (Figure 9b). CitcomSVE results for harmonic at $l = 2$ and $m = 1$ that corresponds to the polar wander also show relatively large differences from each other (Figure 9c), compared with other long-wavelength radial displacements (Figure 9a), although the amplitudes for the polar wander mode are also much smaller. Similar to what we observe for errors in the spatial domain (Table 4), a case with a higher spatial resolution (e.g., Case GIA_R3) is in a better agreement with the semi-analytical solution with a smaller error, but the solutions are insensitive to time resolution Δt (Figures 9b and 9c). To quantify the differences or errors between solutions from those two methods, the time-integrated relative error of degree amplitude for a given degree l is defined by averaged root mean square (RMS) values over the calculation period,

$$\varepsilon_l = \sqrt{\frac{\int_0^T \left[a_{l_{FE}}(t) - a_{l_S}(t)\right]^2 \mathrm{d}t}{\int_0^T a_{l_S}(t)^2 \mathrm{d}t}}, \tag{50}$$

where $a_{l_{FE}}$ and a_{l_S} represent the degree amplitude at time t from the CitcomSVE and semi-analytic method, respectively, and T is the entire calculation period.

The time-integrated errors confirm that a higher spatial resolution leads to smaller errors but the errors are insensitive to temporal resolution (i.e., for Δt from 50 to 250 years) (Table 5). Specifically, for Case GIA_R3 with the highest spatial resolution, the error is <0.2% for $l < 10$, ~0.7% for $l = 16$, and ~2% for $l = 23$. For Case GIA_R1 with the lowest spatial resolution, the error is <1% for $l < 10$, but can reach to 4% for $l = 16$% and 8% for

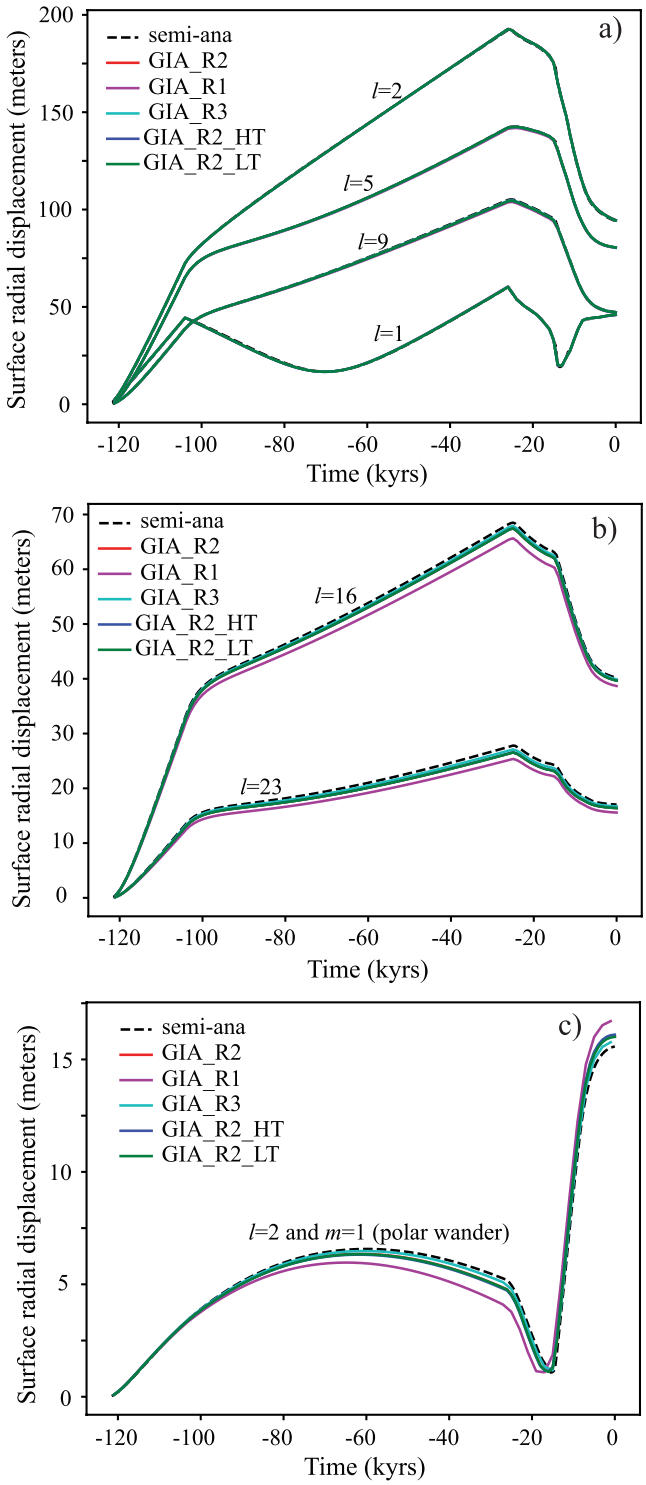

Figure 9. Degree amplitudes of cumulative radial surface displacement at different spherical harmonic degree l as a function of time for the semi-analytical solutions (semi-ana) and five CitcomSVE models: Cases GIA_R1, GIA_R2, GIA_R3, GIA_R2_HT, and GIA_R2_LT: for $l = 1$, 2, 5, and 9 (a), $l = 16$ and 23 (b), and polar wander mode with $l = 2$ and $m = 1$ (c).

$l = 23$ (Table 5). The errors for the polar wander mode with $l = 2$ and $m = 1$ are larger; the errors are ~0.6% and ~5% for Cases GIA_R3 and GIA_R1, respectively.

Figure 10 show relative sea-level (RSL) changes for the last 20,000 years at four sites (two in North America and two in Fennoscandia, see Peltier et al. (2015) for locations of these four sites) from the five CitcomSVE cases and the semi-analytical solutions, together with the observations. While all the CitcomSVE cases reproduce the RSL from the semi-analytical solutions reasonably well, it is evident that higher spatial resolution models (e.g., GIA_R3) are in a better agreement with the semi-analytical solutions and that temporal resolution does not affect the results in any significant way. This is again consistent with what have been observed for errors in spatial and spherical harmonic domains (Tables 4 and 5).

3.4. Efficiency of Parallel Computation of CitcomSVE

Zhong et al. (2008) reported that CitcomS achieves 71% and 57% efficiency in parallel computation for using 1,536 cores and 3,072 cores, respectively, for a convection problem with a fixed grid size per core (i.e., 32^3 elements per core) on Parallel Supercomputer Ranger at the University of Texas' Supercomputer Center. Here, we will perform a similar parallel efficiency benchmark on Parallel Supercomputer Cheyenne at National Center for Atmospheric Research (NCAR). First, we report CPU times used to compute those GIA example problems in last section. As discussed in Section 3.3, Cases GIA_R1, GIA_R2, and GIA_R3 employ grids $12 \times (48 \times 48 \times 48)$, $12 \times (48 \times 80 \times 80)$, and $12 \times (64 \times 128 \times 128)$, respectively, corresponding to surface horizontal grid resolution of 136, 81, and 51 km, respectively. These three cases are computed for 1,220 time-steps with time increment Δt of 100 years per time-step to cover 122 ky glaciation/deglaciation cycle at a convergence tolerance of 3×10^{-3} for iteration solution of the equation of motion. These three cases, all using 96 cores for parallel computing, are computed for 0.345, 1.23, and 4.58 hr, respectively, to their completion (Table 4). These CPU times are approximately proportional to the number of elements for these three cases, suggesting efficient parallel computing in CitcomSVE. Note that if $\Delta t = 250$ years is used (producing similarly accurate solutions) we expect that the CPU times will be halved.

To determine parallel efficiency, we compute the same GIA problem as in last section using a different number of CPU cores from 12 to 6,144 (Table 6). For each test calculation, the number of elements per core is fixed at 32^3, similar to that in Zhong et al. (2008). Therefore, as the number of cores increases, the total number of elements also increases (Table 6). The calculation with 6,144 cores uses a total of 200 million elements with a horizontal resolution of 25 km and a radial resolution of 11 km. For each test calculation, we only compute for the first time step (i.e., the elastic solution) and record the number of iterations for gravitational, pressure and velocity iterations and the CPU time used for this time step (Table 6). Note that the total number of iterations and total CPU time for each calculation are not very meaningful, because they depend on geometrical configuration of an element or grid and other factors. As in Zhong et al. (2008), we compute CPU time per velocity iteration for each calculation and use it to determine the parallel efficiency. These test calculations indicate that CitcomSVE's parallel computing efficiency is quite high, mostly above 75% even for using 6,144 cores, except for 3,072 cores case that yields 66% efficiency.

Table 5
Relative Errors for GIA Surface Radial Displacements at Different Harmonics

(%)	GIA_R1	GIA_R2	GIA_R3	GIA_R2_HT	GIA_R2_LT
ε_1	0.0128	0.0758	0.0974	0.0615	0.0480
ε_2	0.259	0.247	0.198	0.111	0.0689
ε_{2_1} [a]	5.49	1.91	0.64	1.44	1.46
ε_5	0.257	0.107	0.103	0.155	0.123
ε_9	0.893	0.394	0.187	0.764	0.723
ε_{16}	3.88	1.31	0.692	1.56	1.53
ε_{23}	8.44	4.07	2.14	4.27	4.25

[a] ε_{2_1} is the time-integrated error in percentage for $l = 2$ and $m = 1$.

4. Conclusion and Discussion

This study presents an updated finite element package CitcomSVE for modeling deformational response of a planetary mantle with viscoelastic rheology to surface and tidal loading, together with a complete description of the finite element formulation for load-induced dynamic deformation and of computations of the relevant geophysical processes and outputs including the sea-level change, polar wander, apparent center of mass motion, and removal of mantle net rotation. Compared with the earlier version, the updated CitcomSVE can run efficiently on a massively parallel computer with thousands of CPU cores. Extensive benchmark calculations are performed using CitcomSVE and the solutions are compared with semi-analytical solutions to validate the CitcomSVE package. Three benchmark problems are solved with different numerical resolutions: (a) surface loading of different single harmonics, (b) tidal loading at degree 2, and (c) GIA model with ICE 6G and VM5A. Different from our previous benchmark effort (e.g., A et al., 2013; Kang et al., 2022; Paulson et al., 2005; Zhong et al., 2003) that have focused mostly on radial displacement and its associated geophysical quantities (e.g., gravity anomalies and RSL), the current benchmark study considers additionally calculations and comparison of horizontal displacements and displacement rates.

The benchmark calculations demonstrate that CitcomSVE is effective and accurate for solving GIA and tidal loading problems. For example, for a typical GIA calculation with ICE-6G ice model for 122 ky glaciation and

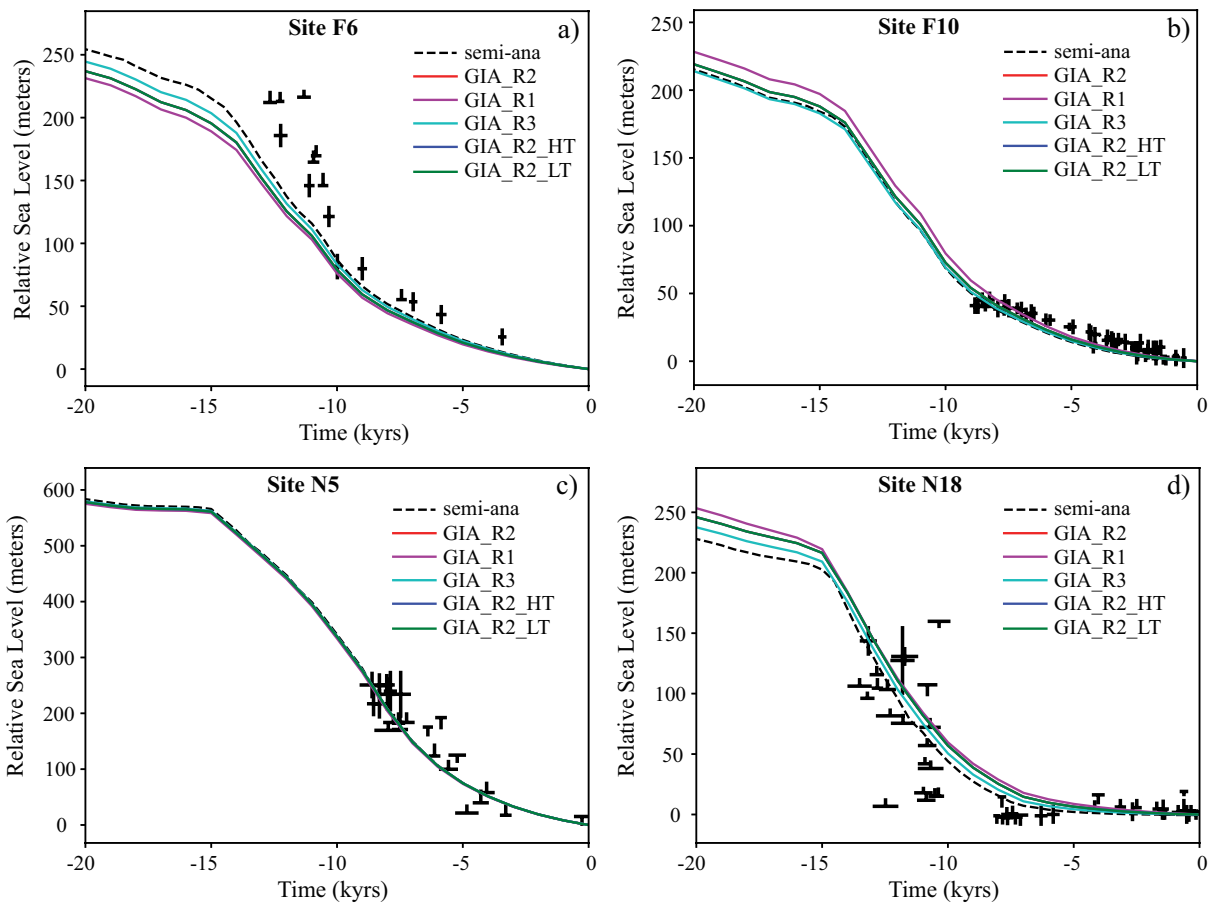

Figure 10. Relative sea level change for the last 20 ky at four different sites from semi-analytical solutions (semi-ana) and five CitcomSVE models: Cases GIA_R1, GIA_R2, GIA_R3, GIA_R2_HT, and GIA_R2_LT. The Sites are F6 (a) and F10 (b) for Fennoscandia and N5 (c) and N18 (d). The symbols represent the observed RSL changes. The sites and the observed RLS are from Peltier et al. (2015).

Table 6
CPU Time With Different Number of Cores

N_c[a]	Grid per cap (12x)	CPU time[b] (sec)	Iterations[c] ($g/p/v$)	CPU time per v-iteration[d] (sec)	Efficiency (%)
12 (1 × 1 × 1)	32 × 32 × 32	6.45	7/32/56	0.115	100
24 (2 × 1 × 1)	64 × 32 × 32	10.4	8/36/89	0.117	98.3
48 (1 × 2 × 2)	32 × 64 × 64	6.00	7/31/44	0.136	84.6
96 (2 × 2 × 2)	64 × 64 × 64	7.90	7/34/57	0.138	83.3
192 (1 × 4 × 4)	32 × 128 × 128	8.01	7/33/57	0.141	81.6
384 (2 × 4 × 4)	64 × 128 × 128	6.67	8/33/44	0.152	75.7
768 (4 × 4 × 4)	128 × 128 × 128	7.93	8/35/54	0.147	78.2
1,536 (2 × 8 × 8)	64 × 256 × 256	8.87	8/34/61	0.145	79.3
3,072 (4 × 8 × 8)	128 × 256 × 256	20.4	9/74/118	0.173	66.5
6,144 (8 × 8 × 8)	256 × 256 × 256	13.6	12/51/94	0.145	79.3

[a]N_c stands for the number of cores. The numbers in the parentheses represent the domain decomposition in each of 12 spherical caps for CitcomSVE. For example, 2 × 2 × 2 indicates that each cap is further divided into two in each of the three directions with the first number for the radial direction. [b]CPU time in second for the zeroth time step of the calculation. [c]The number of iterations for gravitational (g), pressure (p) and velocity (v) iteration levels. [d]CPU time divided by number of v-iterations, which is used to compute the efficiency.

deglaciation history, time increment of 100 years (i.e., 1,220 time steps), ∼50 km (or ∼0.5°) horizontal resolution (i.e., 12 million elements or 39 million degrees of freedom) at the surface, it takes approximately 4.5 hr on 96 cores to complete. The global spatial errors are about 1% and 5% for present-day cumulative displacements and displacement rates, respectively, and the errors for horizontal and radial components are comparable. The errors are smaller for earlier times (e.g., at ∼15 and 26 kybp) and for long-wavelengths (e.g., <1% for spherical harmonic degree $l < \sim 20$). Because gravitational potential calculations are computationally expensive at short wavelengths, for GIA calculations in CitcomSVE, the potential is only computed up to degrees and orders 32. This may have contributed to some of the errors, given that the semi-analytical solutions are computed up to degrees and orders 100. Wang and Li (2021) used a direct integration method to compute the potential, and future studies may explore the efficacy of this method in CitcomSVE for GIA modeling.

Error analyses for calculations with different spatial and temporal resolutions demonstrate that CitcomSVE achieves a second order accuracy with respect to spatial resolution, as expected for the trilinear elements used in CitcomSVE, with exception for very long-wavelengths at $l = 1$ and 2 for which the errors are insensitive to grid resolution and are likely controlled by convergence criteria. The second order accuracy for spatial resolution indicates that the Uzawa algorithm and full multi-grid solvers in CitcomSVE are stable and efficient. The results show that shorter wavelength deformation requires more spatial resolution to be computed accurately, as expected. It is also found that calculations of deformation associated with the polar wander (i.e., at $l = 2$ and $m = 1$) are less accurate, especially for horizontal displacements. The errors for the polar wander mode, although with $l = 2$ it is a long-wavelength feature, are comparable with those at $l \sim 16$. However, moderately high horizontal resolution (∼50 km) is sufficient to cut the errors down to ∼1%. The benchmark calculation on the polar wander is generally consistent with our previous work using CitcomSVE (e.g., Paulson et al., 2005; A et al., 2013).

Our calculations also demonstrate that the errors for both cumulative displacements and displacement rates are insensitive to temporal resolution or time increment Δt, which is surprising. More specifically, our GIA calculations with $\Delta t = 250$ years have similar errors to those with $\Delta t = 50$ and 100 years, and horizontal displacement errors with $\Delta t = 50$ years are even larger than those with $\Delta t = 250$ years. Zhong et al. (2003) reported for the early version of CitcomSVE that the errors for radial displacements and rates are smaller for smaller time increment Δt. The difference may be caused by how the gravitational potential is calculated between these two different versions of the code. In the early version, to reduce computational cost, the gravitational potential, except for the first few time steps, is considered as the same from the previous time step with no iteration to feedback to the displacement solutions (Zhong et al., 2003). However, this cost-saving approximation is removed in the current version such that the gravitational potential is always self-consistently calculated with the displacement via

iteration. Our results suggest that for GIA modeling using ICE-6G ice model in CitcomSVE, tune increment Δt ranging from 100 to 250 years is optimal and gives similar errors. Given that each deglaciation stage in ICE-6G has a time interval of 500 years, we did not test $\Delta t > 250$ years. Clearly, when Δt is sufficiently large, the errors would become larger for larger Δt, especially for the displacement rates. The error insensitivity to time increment Δt suggests that the error for these calculations is likely limited by other factors (e.g., the convergence tolerance level) and not Δt. This is similar to how the errors are insensitive to spatial resolution for long-wavelength loading as discussed earlier (e.g., Figure 5). This issue deserves further studies with different ice models and different viscosity structures, both of which likely affect the choice of Δt.

Our test calculations show that the parallel computation efficiency of CitcomSVE is generally >75% for using up to 6,144 CPU cores with a grid of 200 million elements. Although the current study only considers 3-D spherical models with an incompressible mantle, CitcomSVE package has the capability for modeling a compressible mantle in 3-D spherical geometry (A et al., 2013) and in 3-D regional spherical and Cartesian models (Bellas et al., 2020; Zhong & Watts, 2013), with similar accuracy and efficiency. With its accuracy, fast computational speed, parallel efficiency, and its open-source public availability, CitcomSVE provides a powerful computational tool for modeling viscoelastic deformation of a planetary mantle in response to surface and tidal loading including GIA.

Data Availability Statement

The CitcomSVE package and input files including ICE-6G for this study can be accessible at https://zenodo.org/record/6579345#.Yo3ZXmBBw6E. The updated CitcomSVE package can be downloaded from https://github.com/shjzhong/CitcomSVE. The original ICE-6G ice history model is from https://www.atmosp.physics.utoronto.ca/~peltier/data.php. Other model input parameters are given in Tables 1–4.

Acknowledgments
We dedicate this study to our friend, colleague, and mentor Late Professor John Wahr who had provided invaluable contribution to CitcomSVE's development and continues to be inspiration to our work. We are grateful to Dr. Erik Ivins, Volker Klemann, and an anonymous reviewer for their careful reviews of this highly technical and tedious paper. This work is supported by grants NASA ESI 80NSSC18K0470 and NSF EAR-1940026. Our calculations were performed on parallel computer Cheyenne which is operated by the National Center for Atmospheric Research.

References

A, G., Wahr, J., & Zhong, S. J. (2013). Computations of the viscoelastic response of a 3-D compressible Earth to surface loading: An application to glacial isostatic adjustment in Antarctica and Canada. *Geophysical Journal International*, *192*, 557–572. https://doi.org/10.1093/gji/ggs030

Bagge, M., Klemann, V., Steinberger, B., Latinović, M., & Thomas, M. (2021). Glacial-isostatic adjustment models using geodynamically constrained 3D Earth structures. *Geochemistry, Geophysics, Geosystems*, *22*(11), e2021GC009853. https://doi.org/10.1029/2021GC009853

Becker, T. W. (2006). On the effect of temperature and strain-rate dependent viscosity on global mantle flow, net rotation, and plate-driving forces. *Geophysical Journal International*, *167*, 943–957. https://doi.org/10.1111/j.1365-246x.2006.03172.x

Bellas, A., & Zhong, S. J. (2021). Seismic strain rate and flexure at the Hawaiian Islands constrain the fictional coefficient. *Geochemistry, Geophysics, Geosystems*, *22*, e2020GC009547. https://doi.org/10.1029/2020GC009547

Bellas, A., Zhong, S. J., & Watts, A. B. (2020). Constraints on the rheology of the lithosphere from flexure of the Pacific Plate at the Hawaiian Islands. *Geochemistry, Geophysics, Geosystems*, *21*, e2019GC008819. https://doi.org/10.1029/2019GC008819

Dahlen, F. A., & Tromp, J. (1998). *Theoretical global seismology*. Princeton University Press.

Dziewonski, A. M., & Anderson, D. L. (1981). Preliminary reference Earth model. *Physics of the Earth and Planetary Interiors*, *25*(4), 297–356. https://doi.org/10.1016/0031-9201(81)90046-7

Farrell, W. E., & Clark, J. A. (1976). On postglacial sea level. *Geophysical Journal of the Royal Astronomical Society*, *46*, 647–667. https://doi.org/10.1111/j.1365-246x.1976.tb01252.x

Hager, B. H., & O'Connell, R. J. (1981). A simple global model of plate dynamics and mantle convection. *Journal of Geophysical Research*, *86*, 4843–4878. https://doi.org/10.1029/jb086ib06p04843

Han, D., & Wahr, J. (1995). The viscoelastic relaxation of a realistically stratified earth, and a further analysis of postglacial rebound. *Geophysical Journal International*, *120*, 287–311. https://doi.org/10.1111/j.1365-246x.1995.tb01819.x

Hetland, E. A., & Hager, B. H. (2005). Postseismic and interseismic displacements near a strike-slip fault: A two-dimensional theory for general linear viscoelastic rheologies. *Journal of Geophysical Research*, *110*, B10401. https://doi.org/10.1029/2005JB003689

Hu, Y., & Wang, K. (2012). Spherical-Earth finite element model of short-term postseismic deformation following the 2004 Sumatra earthquake. *Journal of Geophysical Research*, *117*, B05404. https://doi.org/10.1029/2012JB009153

Hughes, T. J. R. (2000). *The finite element method* (p. 682). Dover Publications, Inc.

Ivins, E. R., Caron, L., Adhikari, S., & Larour, E. (2022). Notes on a compressible extended Burgers model of rheology. *Geophysical Journal International*, *228*, 1975–1991. https://doi.org/10.1093/gji/ggab452

Kang, K. S., Zhong, S. J., Geruo, R., Mao, W., & Geruo, A. (2022). The effects of non-Newtonian rheology in the upper mantle on relative sea level change and geodetic observations induced by glacial isostatic adjusted process. *Geophysical Journal International*, *228*, 1887–1906. https://doi.org/10.1093/gji/ggab428

Kendall, R. A., Mitrovica, J. X., & Milne, G. A. (2005). On post-glacial sea level—II. Numerical formulation and comparative results on spherically symmetric models. *Geophysical Journal International*, *161*, 679–706. https://doi.org/10.1111/j.1365-246X.2005.02553.x

Klemann, V., Martinec, Z., & Ivins, E. R. (2008). Glacial isostasy and plate motion. *Journal of Geodynamics*, *46*(3–5), 95–103. https://doi.org/10.1016/j.jog.2008.04.005

Lambeck, K. (1980). *The earth's variable rotation: Geophysical causes and consequences*. Cambridge University Press.

Latychev, K., Mitrovica, J. X., Tromp, J., Tamisiea, M. E., Komatitsch, D., & Christara, C. C. (2005). Glacial isostatic adjustment on 3-D earth models: A finite-volume formulation. *Geophysical Journal International*, *161*, 421–444. https://doi.org/10.1111/j.1365-246x.2005.02536.x

Lau, H. C. P., & Faul, U. (2019). An elasticity from seismic to tidal timescales: Theory and observations. *Earth and Planetary Science Letters*, *508*, 18–29. https://doi.org/10.1016/j.epsl.2018.12.009

Lau, H. C. P., Mitrovica, J. X., Davis, J. L., Tromp, J., Yang, H. Y., & Al-Attar, D. (2017). Tidal tomography constrains earth's deep-mantle buoyancy. *Nature*, *551*, 321–326. https://doi.org/10.1038/nature24452

Li, T., Wu, P., Wang, H., Steffen, H., Khan, N. S., Engelhart, S. E., et al. (2020). Uncertainties of glacial isostatic adjustment model predictions in North America associated with 3D structure. *Geophysical Research Letters*, *47*(10), 1–10. https://doi.org/10.1029/2020GL087944

Longman, I. M. (1966). Computation of Love numbers and load deformation coefficients for a model earth. *Geophysical Journal International*, *11*, 133–137. https://doi.org/10.1111/j.1365-246x.1966.tb03495.x

Martinec, Z. (2000). Spectral–finite element approach for three-dimensional viscoelastic relaxation in a spherical earth. *Geophysical Journal International*, *142*, 117–141. https://doi.org/10.1046/j.1365-246x.2000.00138.x

Martinec, Z., Klemann, V., van der Wal, W., Riva, R. E. M., Spada, G., Sun, Y., et al. (2018). a benchmark study of numerical implementations of the sea level equation in gia modelling. *geophysical journal international*, *215*, 389–414. https://doi.org/10.1093/gji/ggy280

Milne, G. A. (1998). *Refining models of the glacial isostatic adjustment process, PhD thesis*. University of Toronto.

Mitrovica, J. X., Wahr, J., Matsuyama, I., & Paulson, A. (2005). The rotational stability of an ice-age earth. *Geophysical Journal International*, *161*(2), 491–506. https://doi.org/10.1111/j.1365-246X.2005.02609.x

Moresi, L. N., & Solomatov, V. S. (1995). Numerical investigation of 2D convection with extremely large viscosity variation. *Physics of Fluids*, *9*, 2154–2164. https://doi.org/10.1063/1.868465

Moresi, L. N., Zhong, S. J., & Gurnis, M. (1996). The accuracy of finite element solutions of Stokes' flow with strongly varying viscosity. *Physics of the Earth and Planetary Interiors*, *97*, 83–94. https://doi.org/10.1016/0031-9201(96)03163-9

Nur, A., & Mavko, G. (1974). Postseismic viscoelastic rebound. *Science*, *183*, 204–206. https://doi.org/10.1126/science.183.4121.204

Paulson, A., Zhong, S. J., & Wahr, J. (2005). Modeling post-glacial rebound with lateral viscosity variations. *Geophysical Journal International*, *163*, 357–371. https://doi.org/10.1111/j.1365-246x.2005.02645.x

Paulson, A., Zhong, S. J., & Wahr, J. (2007). Limitations on the inversion for mantle viscosity from post-glacial rebound. *Geophysical Journal International*, *168*(3), 1195–1209. https://doi.org/10.1111/j.1365-246x.2006.03222.x

Peltier, W. R. (1976). Glacial-isostatic adjustment B II. The inverse problem. *Geophysical Journal of the Royal Astronomical Society*, *46*, 669–705.

Peltier, W. R., Argus, D. F., & Drummond, R. (2015). Space geodesy constrains ice age terminal deglaciation: The global ICE-6G_C (VM5a) model. *Journal of Geophysical Research: Solid Earth*, *120*, 450–487. https://doi.org/10.1002/2014JB011176

Qin, C., Zhong, S. J., & Phillips, R. (2018). Formation of the lunar fossil bulges and its implication for the early Earth and Moon. *Geophysical Research Letters*, *45*, 1286–1296. https://doi.org/10.1002/2017GL076278

Qin, C., Zhong, S. J., & Wahr, J. (2014). A perturbation method and its application: Elastic tidal response of a laterally heterogeneous planet. *Geophysical Journal International*, *199*, 631–647. https://doi.org/10.1093/gji/ggu279

Qin, C., Zhong, S. J., & Wahr, J. (2016). Elastic tidal response of a laterally heterogeneous planet: A complete perturbation formulation. *Geophysical Journal International*, *207*, 89–110. https://doi.org/10.1093/gji/ggw257

Rollins, C., Freymueller, J. T., & Sauber, J. M. (2021). Stress promotion of the 1958 $M_w \sim 7.8$ fairweather fault earthquake and others in southeast Alaska by glacial isostatic adjustment and inter-earthquake stress transfer. *Journal of Geophysical Research: Solid Earth*, *126*, e2020JB020411. https://doi.org/10.1029/2020JB020411

Schubert, G., Turcotte, D. L., & Olson, P. (2001). *Mantle convection in the Earth and planets*. Cambridge University Press.

Spada, G., Barletta, V. R., Klemann, V., Riva, R. E. M., Martinec, Z., Gasperini, P., et al. (2011). A benchmark study for glacial isostatic adjustment codes. *Geophysical Journal International*, *185*, 106–132. https://doi.org/10.1111/j.1365-246X.2011.04952.x

Takeuchi, H. (1950). On the Earth tide of the compressible Earth of variable density and elasticity. *Transactions American Geophysical Union*, *5*, 651–689. https://doi.org/10.1029/tr031i005p00651

Tan, E., Leng, W., Zhong, S. J., & Gurnis, M. (2011). On the location of plumes and lateral movement of thermo-chemical structures with high bulk modulus in the 3-D compressible mantle. *Geochemistry, Geophysics, Geosystems*, *12*, Q07005. https://doi.org/10.1029/2011GC003665

van der Wal, W., Barnhoorn, A., Stocchi, P., Gradmann, S., Wu, P., Drury, M., & Vermeersen, B. (2013). Glacial isostatic adjustment model with composite 3-D Earth rheology for Fennoscandia. *Geophysical Journal International*, *194*(1), 61–77.

Wahr, J., Selvans, Z. A., Mullen, M. E., Barr, A. C., Collins, G. C., Selvans, M. M., & Pappalardo, R. T. (2009). Modeling stresses on satellites due to nonsynchronous rotation and orbital eccentricity using gravitational potential theory. *Icarus*, *200*(1), 188–206. https://doi.org/10.1016/j.icarus.2008.11.002

Wang, Y. M., & Li, M. M. (2021). The interaction between mantle plumes and lithosphere and its surface expressions: 3-D numerical modelling. *Geophysical Journal International*, *225*, 906–925. https://doi.org/10.1093/gji/ggab014

Watts, A. B. (2001). *Isostasy and flexure of the lithosphere*. Cambridge University Press.

Wu, P. (2004). Using commercial finite element packages for the study of Earth deformations, sea levels and the state of stress. *Geophysical Journal International*, *158*(2), 401–408. https://doi.org/10.1111/j.1365-246X.2004.02338.x

Wu, P., & Peltier, W. R. (1982). Viscous gravitational relaxation. *Geophysical Journal International*, *70*(2), 435–485. https://doi.org/10.1111/j.1365-246X.1982.tb04976.x

Zhong, S. J. (2001). Role of ocean-continent contrast and continental keels on plate motion, net rotation of lithosphere and the geoid. *Journal of Geophysical Research*, *106*, 703–712. https://doi.org/10.1029/2000jb900364

Zhong, S. J., McNamara, A. K., Tan, E., Moresi, L., & Gurnis, M. (2008). A benchmark study on mantle convection in a 3-D spherical shell using CitcomS. *Geochemistry, Geophysics, Geosystems*, *9*, Q10017. https://doi.org/10.1029/2008GC002048

Zhong, S. J., Paulson, A., & Wahr, J. (2003). Three-dimensional finite element modeling of Earth's viscoelastic deformation: Effects of lateral variations in lithospheric thickness. *Geophysical Journal International*, *155*, 679–695. https://doi.org/10.1046/j.1365-246x.2003.02084.x

Zhong, S. J., Qin, C., Geruo, A., & Wahr, J. (2012). Can tidal tomography be used to unravel the long-wavelength structure of the lunar interior? *Geophysical Research Letters*, *39*, L15201. https://doi.org/10.1029/2012GL052362

Zhong, S. J., & Watts, A. B. (2013). Lithospheric deformation induced by loading of the Hawaiian Islands and its implications for mantle rheology. *Journal of Geophysical Research*, *118*, 6025–6048. https://doi.org/10.1002/2013JB010408

Zhong, S. J., Yuen, D. A., & Moresi, L. N. (2007). Numerical methods in mantle convection. In G. Schubert (Ed.) *Treatise in geophysics* (Vol. *7*, pp. 227–252).

Zhong, S. J., & Zuber, M. T. (2000). Long-wavelength topographic relaxation for self-gravitating planets and its implications to the compensation of lunar basins. *Journal of Geophysical Research*, *105*, 4153–4164. https://doi.org/10.1029/1999je001075

Zhong, S. J., Zuber, M. T., Moresi, L., & Gurnis, M. (2000). Role of temperature-dependent viscosity and surface plates in spherical shell models of mantle convection. *Journal of Geophysical Research: Solid Earth*, *105*, 11063–11082. https://doi.org/10.1029/2000JB900003